Experimental and computational evidence of U(VI)–OH–$Si(OH)_4$ complexes under alkaline conditions: Implications for cement systems

Chengming Shang [a,*], Xavier Gaona [a,**], Hanna Oher [b], Robert Polly [a], Andrej Skerencak-Frech [a], Sarah Duckworth [a], Marcus Altmaier [a]

[a] Institute for Nuclear Waste Disposal (INE), Karlsruhe Institute of Technology (KIT), 76344 Eggenstein-Leopoldshafen, Germany
[b] Laboratoire de Physique des 2 Infinis Irène Juliot-Curie (IJCLab), CNRS/IN2P3, Université Paris-Saclay, 91405 Orsay, France

HIGHLIGHTS

- Formation of U(VI)–OH–$Si(OH)_4$ complexes proposed in alkaline conditions.
- Thermodynamic information and luminescent properties were acquired for $UO_2(OH)_2SiO(OH)_3^-$ and $UO_2(OH)_2SiO_2(OH)_2^{2-}$.
- Bidentate silicate in the inner sphere of uranyl moiety was identified by quantum chemical calculations in $UO_2(OH)_2SiO(OH)_3^-$.
- The presence of $UO_2(OH)_2SiO(OH)_3^-$ was identified in the most degraded state of cement.

GRAPHICAL ABSTRACT

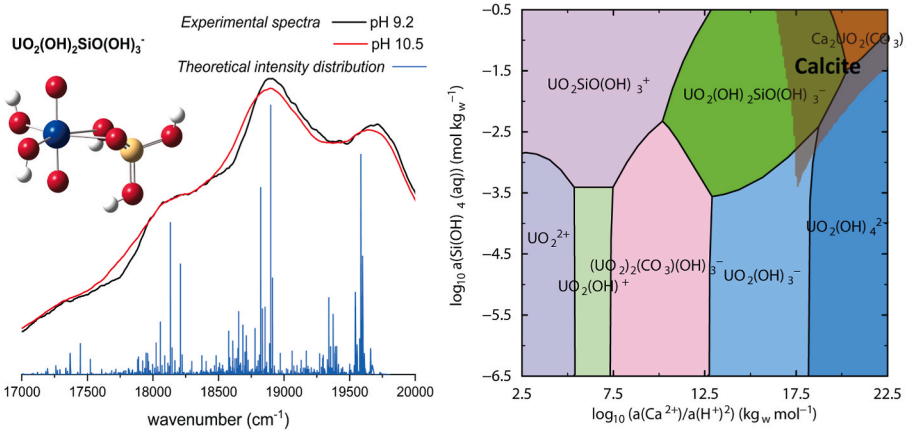

ABSTRACT

The complexation of uranyl hydroxides with orthosilicic acid was investigated by experimental and theoretical methods. Spectroluminescence titration was performed in a glovebox under argon atmosphere at pH 9.2, 10.5 and 11.5, with [U(VI)] 10^{-6} and 5×10^{-6} mol kg_w^{-1}. The polymerization effects of silicic acid were minimized by ruling out samples with less than 90 % monomeric silicic acid present, identified via UV–Vis spectrometry using the molybdate blue method. Linear regression analysis based on time-resolved laser-induced fluorescence spectroscopy (TRLFS) results yielded the conditional stepwise formation constants of U(VI)–OH–$Si(OH)_4$ complexes at 0.05 mol kg_w^{-1} $NaNO_3$. The main spectroscopic features – characteristic peak positions and decay-time – are reported for the first time for the $UO_2(OH)_2SiO(OH)_3^-$ species observed at pH 9.2 and 10.5 and $UO_2(OH)_2SiO_2(OH)_2^{2-}$ predominant at pH 11.5. Quantum chemical calculations successfully computed the theoretical luminescence spectrum of the complex $UO_2(OH)_2SiO(OH)_3^-$ species, thus underpinning the proposed chemical model for weakly alkaline systems. The conditional stability constants were extrapolated to infinite

Keywords:
Uranium(VI)
Silicate
TRLFS
Thermodynamics
DFT
Cement systems

* Corresponding author.
** Corresponding author.
E-mail addresses: chengming.shang@kit.edu (C. Shang), xavier.gaona@kit.edu (X. Gaona).

dilution using the Davies equation, resulting in $\log_{10}\beta^{\circ}(UO_2(OH)_2SiO(OH)_3^-)$ and $\log_{10}\beta^{\circ}(UO_2(OH)_2SiO_2(OH)_2^{2-})$. Implications for U(VI) speciation in the presence and absence of competing carbonate are discussed for silicate-rich environments expected in certain repository concepts for nuclear waste disposal.

1. Introduction

Uranium is a radionuclide found in different environmental components (water, soil, sediment) as a result of mining activities, weapons testing and manufacturing, use of phosphates in agriculture, among others (Riley, 1992; Bernhard et al., 1996; Morris et al., 1996; Bostick et al., 2002; Wang et al., 2004, 2005b; Drozdzak et al., 2016). Large inventories of uranium are found in nuclear wastes arising from different applications (especially energy production), as well as at natural sites where U-rich mineralizations have formed after long-term natural geologic or/and hydrologic processes (Payne and Waite, 1991; Duff et al., 1997, 2000; Hunter and Bertsch, 1998). The omnipresence of silicon in the environment in different forms of monomeric, polymeric or colloidal silicate species can significantly influence the speciation of uranium, which largely controls its partitioning with the solid phase (Payne and Waite, 1991; Waite et al., 1994; Duff and Amrhein, 1996; Davis et al., 1998). In the context of clay formations as well as in cementitious systems considered in several repository concepts (especially for low and intermediate level wastes, L/ILW), the potential formation of stable U(VI)–OH–$Si(OH)_4$ complexes can play an important role in the possible mobilization of uranium (Miller et al., 2000; Alexander et al., 2015). In the context of vitrified high-level wastes (HLW), the dissolution of borosilicate glasses can be considered as an additional source of silicon interacting with the radionuclides (Grambow, 2006). Among others, uranyl silicate precipitates belonging to the uranophane [$Ca(UO)_2SiO_3(OH)_2 \bullet 5H_2O$] and/or boltwoodite [$K(UO_2)(SiO_3OH)(H_2O)_{1.5}$] group of minerals have been identified in subsurface sediments as a result of the alteration and oxidation of primary ore minerals, albeit with uranyl carbonate as major aqueous species in sediment pore waters (Catalano et al., 2004; Liu et al., 2004; Wang et al., 2004, 2005b). Apart from their significance in naturals environments, sodium boltwoodite has been found in the unsaturated zone of the contaminated sediment at Hanford site (Catalano et al., 2004).

Since the 1990's, several studies have investigated the complexation of lanthanides and actinides with silicates and reported their thermodynamic properties, e.g. for Np(IV, V, VI) (Shilov et al., 2004; Yusov et al., 2005), Pu(IV, VI) (Yusov and Fedoseev, 2003), Am(III) (Wadsak et al., 2000; Thakur et al., 2007), Cm(III) (Panak et al., 2005; Wang et al., 2005a), Eu(III) (Jensenf and Choppin, 1996; Pathak and Choppin, 2006; Vercouter et al., 2009b). In particular, various analytical techniques were used to investigate the interaction of U(VI) with orthosilicic acid and the deprotonated H_3SiO_4 in mildly acidic pH conditions, such as time-resolved laser-induced luminescence spectroscopy (Moll et al., 1998; Saito et al., 2015), laser-induced luminescence spectroscopy (Lösch et al., 2020), UV–vis spectrophotometry (Porter and Weber, 1971; Jensenf and Choppin, 1998; Yusov and Fedoseev, 2005) and solvent extraction (Satoh and Choppin, 1992; Hrnecek and Irlweck, 1999; Pathak and Choppin, 2006). Nonetheless, little is known about the formation behaviour of uranium silicate complexes in the alkaline pH range, leaving the thermodynamic data available for geochemical calculations incomplete. One of the challenges faced by these studies relates to the uncertainties affecting the degree of polymerization and polymerization kinetics of silicic acid, which often results in the inaccurate interpretation of the experimental observations (Yusov and Fedoseev, 2003, 2005; Vercouter et al., 2009a). Experimental studies investigating the aqueous speciation of silicon in acidic to weakly alkaline pH values support the predominance of the monomeric Si$(OH)_4$(aq) species at total concentrations below the solubility limit of amorphous silica, i.e., 2×10^{-3} M up to pH 9 (Alexander et al., 1954; Bilinski and Ingri, 1967; Iler, 1979; Marshall, 1980; Marshall and Warakomski, 1980; Fleming and Crerar, 1982; Sjöberg, 1996; Reiller et al., 2011; Mysen and Richet, 2018). However, the recent use of novel techniques, such as electrospray ionization mass spectrometry (ESI-MS), suggests that silicate oligomeric species may form in acidic conditions even below the solubility limit of amorphous silica (Lösch et al., 2020). In line with this observation, the panel reviewers of NEA-TDB (the critical review commissioned by the Thermodynamic Data Base project of the Nuclear Energy Agency (NEA) under the Organization for Economic Co-operation and Development (OECD)) also remarked the underestimated polymeric silicate species in previously recommended equilibrium constants of $UO_2SiO(OH)_3^+$ (Grenthe et al., 1992, 2020; Guillaumont et al., 2003). The latest NEA-TDB update book selected the $\log_{10}K^{\circ}(UO_2SiO(OH)_3^+)$ measured at low concentrations of silicic acid that ensured the predominance of monomeric Si$(OH)_4$(aq) (Grenthe et al., 1992, 2020; Guillaumont et al., 2003). However, the scarcity of experimental investigations focusing on the complexation of uranium with silicate at pH > 9 prevented the selection of additional U(VI)–OH–$Si(OH)_4$ complexes expected to form at higher pH conditions. The formation of these complexes can influence the transport and interactions of radionuclides in naturally or artificially high alkaline waters – in lake brines or hot springs (Eugster, 1970; Dietzel, 2000) or in vicinity of a cement-based nuclear waste repository (Eikenberg, 1990; Reiller et al., 2011; Gaona et al., 2012).

Complexation of uranium with silicic acid in more alkaline environment of pH > 9 is challenged by enhanced solubility of amorphous silica and the intricate polymerization of Si, which depends on numerous factors, e.g., pH, temperature, aging time and silicon concentration (Alexander et al., 1954; Greenberg, 1957; Greenberg and Price, 1957; van Lier et al., 1960; Iler, 1979; Schwartzentruber et al., 1987). The high pK_a of 9.81 (Grenthe et al., 1992) for the first dissociation of Si$(OH)_4$(aq) explains the modest increase of solubility below pH 10. Above pH ~10.5, the steep rise of overall silicate solubility is generally explained by the formation of the doubly negative charged monomeric silicate $SiO_2(OH)_2^{2-}$, as well as by the easily triggered polymerization even below/at the solubility limit of amorphous silica (Alvarez and Sparks, 1985; Applin, 1987).

Luminescence spectroscopy has demonstrated its suitability and appropriateness in studying the luminescent properties of aqueous uranyl(VI) in trace quantities (Moulin et al., 1990, 1995), including the faintly detectable uranyl carbonate species in a notable quenching environment such as NaCl (Shang and Reiller, 2020, 2021). Nonetheless, one specific issue is the analytical limitation of laser spectrometry in determining the structures and geometries of uranium compounds. TRLFS especially excels in providing information on the energy levels, electronic structure, and speciation of uranium species in solution. However, this technique is limited in discerning intricate structural details, such as bond length and bond angle. In addition, the interaction of the laser beam with the fluorophore may induce changes in its local environment during a lengthy measurement process, a phenomenon often observed in organic studies (Lakowicz, 2006), potentially influencing the accuracy of structural determinations.

Recently, the theoretical luminescence spectra of $Na_mM_nUO_2(CO_3)_3^{(4-m-2n)}$ (M = Mg, Ca; m, n = 0–2) have been successfully computed using time-dependent density functional theory (TD-DFT) calculations (Oher et al., 2020b). The robustness of calculated data is verified by good agreement with experimental spectra. This approach has proven its capability to accurately reproduce electronic transitions from lower energy excited states by incorporating relativistic effects, spin-orbital coupling and electron correlation into the calculations. The application of TD-DFT enables the prediction of spectral features by

comparing the energies of different electronic states, ultimately facilitating the identification of the relevant species contributing to the observed luminescence spectra.

The uranyl-hydroxide-silicate system is studied in this work with the objective of determining the formation constants of $UO_2(OH)_xSiO(OH)_3^{1\ x}$ or $UO_2(OH)_ySiO_2(OH)_2^{\ y}$ (x = 1, 2 or 3, y = 2 or 3) under high pH conditions, which have been rarely studied in the literature. Lösch (2020) reported $\log_{10}\beta^\circ(UO_2(OH)_2SiO(OH)_3) = -(17.21 \pm 1.09)$, which was determined within the pH range of 6–11.5 using the Schubert method. This method is based on the difference in partition coefficients of a dissolved species (U(VI)) and a solid phase (ZrO_2) in the presence and absence of the complexing agent (silicate). In addition, extended X-ray absorption spectroscopy (EXAFS) (Mei et al., 2015), X-Ray Photoelectron Spectroscopy (XPS) (Froideval et al., 2006) were used to investigate the atomic structures of uranium-silicate surface species. The application of EXAFS to the investigation of aqueous U(VI)–OH–$Si(OH)_4$ complexes is hindered by the relatively high U(VI) concentration (in the millimolar range) required for accurate structural analysis.

In the current research, we aim to unravel the mechanism behind the complexation behaviour of ternary U(VI)–OH–$Si(OH)_4$ complexes using a combination of experimental and theoretical methods. The dominance of monomeric silicic acid in each sample solution was ensured by systematic cross-checking using the molybdate blue reaction in combination with UV–visible spectrophotometry. The acquisition of U(VI)–OH–$Si(OH)_4$ TRLFS spectra permitted quantitatively measuring the complexation constants of ternary species with gradually enhanced luminescence intensity upon the incorporation of silicic acid into the equatorial plane of uranyl ion. Candidate structures are proposed, with their luminescence spectra optimized through the application of DFT and the luminescence spectra determined with TD-DFT. Special attention is given to the determination of the vibrational levels and the transition intensities between the vibrational levels of the excited and the ground state (Oher et al., 2020b). A comparison between the experimentally acquired and theoretically estimated spectra allows us to gain a deeper understanding of the characteristic band positions originating from different electronic transitions. The use of DFT and TD-DFT offers a practical solution that enables accurate calculations while minimizing the computational burden because of the large uranium assemblies. Practical applications of the chemical and thermodynamic models derived in this work are considered in the context of cementitious environments of relevance in specific repository concepts for nuclear waste disposal. The importance of U(VI)–OH–$Si(OH)_4$ complexes is highlighted in the most degraded state of cement phases, whereas the strong complexing ability of carbonate with uranyl constrains their prevalence in natural groundwater systems.

2. Experimental

2.1. Reagents and solution

All concentrations are expressed in molal units to avoid deviations from temperature-dependent aqueous density. The selection of the electrolyte and its concentration is a critical aspect in reducing the presence of polymeric silicate species and optimizing the performance of the laser device. The background of 0.05 mol kg_w^{-1} $NaNO_3$ was selected for the following reasons: (i) there is a need to ensure a low electrolyte concentration to achieve high pH values while minimizing the polymerization of silicic acid, which increases with pH and ionic strength. The goal is to achieve the desired pH without potential impurities from the formation of polysilicates (Thakur et al., 2007); (ii) the use of excitation wavelength at 266 nm may lead to interferences between excited states of perchlorate and those of the radionuclides. This interference has been observed in the case of Eu(III) but is not specific to it (Vercouter, 2005); (iii) without prior scientific assurances, the unknown luminescence of uranyl hydroxides silicate species can be largely attenuated by the quenching effects of chloride, thus precluding the use of NaCl as background electrolyte.

A stock solution of U(VI) was prepared by dissolving well-characterised $UO_2(NO_3)_2 \bullet 6H_2O$ in 0.01 *m* HNO_3 (Aldrich). Anhydrous $NaNO_3$ (Merck-Emsure) was used to prepare the inert electrolyte. The stock solutions of sodium silicate (0.1 and 0.2 *m*) were freshly prepared by dissolving required quantities of silicon dioxide (Aerosil® 200 Pharma) in 1.0 M NaOH (Titrisol@ Merck) for at least 24 h to decompose possible polymeric species. Purified Millipore deionized water (Milli-Q Advantage A10, 18.2 MΩ cm^{-1}) with Millipore Millipak® 40 filter 0.22 μm was used throughout the sample preparation. All liquid stock solutions were purged with argon for 30 min to remove traces of O_2 and CO_2 before transferring them into an Ar glovebox with <3 ppm O_2 at (25 ± 2) °C. The prepared sample cuvettes were closed and sealed with Teflon tape inside the glove box and transferred outside for further measurements. To ensure consistency, the time between sample preparation and measurement was carefully monitored to be within the range of 2–3 h for each individual sample. This equilibration time is considered appropriate to ensure full complexation before the induction of polymerization.

The sample solutions were analyzed for U(VI) by inductively coupled plasma mass spectroscopy (ICP-MS) and the analysis for Si was performed using both inductively coupled plasma optical emission spectrometry (ICP-OES) and ICP-MS. The degree of polymerization of orthosilicate acid was determined spectrophotometrically with the molybdate blue method after filtrating the sample solutions with Omega Membrane 10 kD (= 2.5 nm) filters (Microsep@ Pall Corporation) (Coudurier et al., 1971) at 6000 rpm for 5 min (Biofuge Primo, Heraeus Instruments). Phase separation by ultrafiltration excluded any contribution from U(VI) solid phases (e.g., boltwoodite, weeksite, or $Na_2U_2O_7 \bullet H_2O$ (cr)) or polymeric silicates particles. Sample solution was prepared in 10 mL polyethylene bottle and spiked with adequate volumes of 0.1 and 0.2 *m* sodium silicate solutions. Sodium hydroxide (NaOH, Titrisol@ Merck) and nitric acid (HNO_3, Titrisol@ Merck) were freshly prepared to adjust the designed pH values. An Orion™ ROSS combination pH electrode (Thermo Scientific) was standardized using standard buffer solutions of pH 3–11 (Merck). The responses of potential shown on the pH-meter against reference pH values were analyzed by ordinary least squares regression. The pH measurements were thus performed with the uncertainty of below 0.05 pH units, corresponding to 95% confidence limits.

The selection of specific pH values in this study was guided by multiple considerations. Systematic preliminary titration experiments were conducted across a pH range spanning from 9 to 13.5. The pH values – 9.2 and 10.5, were chosen where $UO_2(OH)_3^-$ species predominates (see Fig. S1). At pH > 12, it was found that uranyl hydroxides silicate species was impossible to outcompete hydrolysis – the non-luminescent $UO_2(OH)_4^{2-}$ – at low Si concentrations which was interpreted by signal annihilation in luminescence spectra. Attempts were made by increasing Si concentrations to around 0.1 M. However, undesirable polymeric silicate formations cannot be avoided at such concentrations which can be confirmed by molybdate verification. For this reason, the upper pH limit was capped at 11.5 in this study.

2.2. Time-resolved laser-induced luminescence spectroscopy and data processing

A 2 mL sample solution of uranium(VI) was taken from the 10 mL polyethylene bottle and placed in a 10 × 10 mm quartz cuvette (QS101, Suprasil, Hellma Analytics). Prior to data acquisition, the sample solution was thermally pre-equilibrated at 25 °C in a sample holder connected to a thermostat (D-77656, Peter Huber Kältemaschinenbau AG, Germany) with circulating water to minimize temperature fluctuations on uranium fluorescence (Moriyasu et al., 1977). The TRLFS measurements were conducted using a pulsed Nd: YAG laser (SpitLight Compact 100, Innolas Laser) with crystals for the 4th harmonic generation at 266 nm. The excitation source delivers energy of about 3 mJ at a repetition rate of 10 Hz with 7 ns pulse duration. Two dichroic mirrors are placed

in a 90° configuration relative to the laser beam. Part of the laser beam was sent to a thermopile sensor (1Z02155, Newport Corporation) and the laser energy was read from Ophir LaserStar (1Z01600, Laser Measurement Group). The emission spectra of U(VI) were detected by a time-gated intensified CCD camera (iStar, Kymera 328i-C, Acton Technology). An Andor monochromator spectrometer was used to collect the luminescence signal at 300 lines mm ^{1} grating in this study. The data acquisition by the intensified CCD camera was synchronized with the output signal of the laser system by a digital delay pulse generator (Model DG 535, Stanford Research Systems). The software program SOLIS (4.32.30065, Andor Technology) was used to control the gate delay and gate width of the intensified CCD camera.

In this study, the absorption of species before and after the exciting laser beam flux entering into the detection system, i.e., pre- or post-filter effects were considered negligible at uranium concentration of ($5 \times$) 10^{6} *m* and the luminescence behaviour was cumulative contribution of different uranium(VI) species. The time-resolved luminescent spectra were recorded in the wavelength range from 395 to 655 nm as a function of delay time $D \geq 20$ ns. This temporally resolved mode supported by pulsed excitation and gated detection can enable better distinction between uranium species and noise signal from background constituents. The gate-width was fixed at 500 μs. The evaluation of the acquired spectroscopic data was focused on the characteristic uranium luminescence between 440 and 610 nm. Eq. (1) gives the expression of luminescence signal. The collected spectra were integrated over the investigated wavelength span to deduce the luminescence intensity at different delay times.

$$FI = \sum_{i} FI_0\ \tau_i\ \exp\left(\frac{D}{\tau_i}\right)\left(1 \quad \exp\left(\frac{W}{\tau_i}\right)\right) \tag{1}$$

where τ_i represents luminescence decay time of species *i*, *W* is the gate-width, *FI* is fluorescence intensity at a specific delay time *D* and FI_0 is that at $D = 0$.

The original data were analyzed with OriginPro software by a customised data processing procedure (Origin-2022-9.9, OriginLab Corporation, Northampton MA, USA), which includes background subtraction and peak integration with the trapezoidal rule. The Levenberg-Marquardt algorithm was applied in the least-square curve fittings. For every sample solution, the luminescence decay time as well as intensity at $D = 20$ ns were calculated by fitting the luminescence intensities *FI*(t) at various delay times to an exponential decay function (Moreau et al., 2015; Kouhail et al., 2016, 2019; Fromentin and Reiller, 2018). The luminescence decay time analysis provided complimentary information on the surrounding environment of uranyl ion as well as the complexation configuration of silicate.

2.3. Determination of the monomeric silicic acid fraction

The measurement of aqueous monosilicates content is based on the formation of a yellow beta-molybdosilicic acid by reacting with molybdate at acidic conditions, as expressed in Eq. (2) (Rinder and Oelkers, 2014) which can be reduced to a blue molybdenum complex.

$$7\ Si(OH)_4 + 12\ H_6Mo_7O_{24} \bullet 4\ H_2O + 126\ H_2O - 7\ H_8Si(Mo_2O_7)_6 \bullet 28\ H_2O \tag{2}$$

A series of SiO_2 calibration solutions of concentration from 100 to 1000 mg/l (corresponding to 1.67×10^{3} *m* and 1.67×10^{2} *m*, respectively) were prepared from the SiO_2 stock solution provided in the Silicic Acid Test-kit (Supelco Spectroquant, Sigmaaldrich). The measurements of absorbance were performed at 430 nm with 10 mm pathlength cells (VWR macro cuvette PS No. 634–0675). The responses of absorbance shown on the UV–Visible spectrometer (Genesys™ 20, Thermo Scientific) against SiO_2 calibration solutions were analyzed by means of ordinary least squares to give a multi-point calibration with 95 % confidence limits (Manov et al., 1945; de Levie, 2005). To assess the fraction of monomeric silicic acid in each sample, a new solution was prepared under the absence of uranium at the same silicate concentration and analyzed by ICP-OES. The fraction of monomeric silicic acid was then evaluated by direct spectroscopic measurement according to the predetermined calibration.

2.4. Geochemical modelling

The chemical speciation and predominance diagrams of uranium (VI) were constructed from our newly determined formation constants for U(VI)–OH–$Si(OH)_4$ complexes using PhreeqC and PhreePlot (Parkhurst and Appelo, 1999, 2013; Kinniburgh and Cooper, 2004, 2011) and is further based upon the uranium thermodynamic data from the NEA-TDB database (Grenthe et al., 2020). Table 1 lists the stepwise and global equilibrium constants, $\log_{10}K^{\circ}$ and $\log_{10}\beta^{\circ}$, respectively, for uranium (VI) species. The solubility products of uranium (VI) solid phases – $UO_3{:}2H_2O$ (cr) and $Na_2U_2O_7{:}H_2O$ (cr) – were employed to maintain undersaturation of metaschoepite and sodium uranate during experiments. This was achieved by calculating the saturation indices for each prepared sample. The Gibbs energies of formation were calculated for the major species used in this work, as listed in Table 2.

2.5. Computational details

The three main tasks for the computational part of this work are the determination of the equilibrium structures of the selected complexes, the calculation of the electronic excitation energies and the careful consideration of the vibrational transitions between the electronically excited states and the ground state. The luminescence spectra were simulated using the ezSpectrum 3.0 software (http://iopenshell.usc.edu/downloads/ezspectrum) to complement the experimental approach and validate the U(VI)–OH–$Si(OH)_4$ species. The approach used is thoroughly described in previous studies (Tecmer et al., 2012; Oher et al., 2020a, 2020b, 2022, 2023). The Franck-Condon factors (FCFs), which represent the overlaps between the ground and excited vibrational wave functions, were determined by incorporating Duschinsky rotations to account for potential variations in the normal modes of the considered states. The theoretical luminescent and ground states were configured to have one and three vibrational quanta, respectively, to replicate the number of transitions observed on experimental spectra. The simulations were conducted at a temperature of 298.15 K to align with experimental conditions. The shape of the theoretical spectra was modelled using the Lorentzian-based peak with a full width at the half-maximum of 350 cm ^{1}.

The necessary data for simulating the luminescence spectra of uranyl-hydroxide-silicate species were derived from ab initio packages. The ground and the first excited (luminescent) state geometries were described at the relativistic spin-free level using density functional theory (DFT), with the Kohn-Sham equation solved using the hybrid PBE0 functional of the density (Ernzerhof and Scuseria, 1999). To account for scalar relativistic effects of the 60 core electrons, a small-core Relativistic Effective Core Potential (RECP) was applied to the uranium atom (Küchle et al., 1994; Cao et al., 2002). The valence electrons were described by the def-TZVP basis set (Weigend et al., 1998). The second-generation Karlsruhe basis set def2-TZVP was used for the H, O and Si elements (Weigend and Ahlrichs, 2005). The preliminary chemical models were constructed using resolution of identity DFT (RI-DFT) (BP86/def-TZVP/def2-TZVP) method as implemented in TURBOMOLE (version 7.0, 2015), known for its ability to simplify DFT calculations by replacing the part of integrals with predetermined constants (Schäfer et al., 1992; Eichkorn et al., 1995; Treutler and Ahlrichs, 1995; Eichkorn et al., 1997; von Arnim and Ahlrichs, 1999; Deglmann et al., 2004; Ahlrichs et al., 2015). The time-dependent DFT (TD-DFT) method, implemented in *Gaussian*16 (RevA.03), was then employed to determine the geometries of both ground and excited states. All optimized

Table 1
Stepwise and global equilibrium constants ($\log_{10}K^{\circ}$ and $\log_{10}\beta^{\circ}$) for uranium (VI) species and solubility products of uranium (VI) solid phases, used in this work.

Reaction	$\log_{10} K^{\circ}$	References
$CO_2(g) + H_2O \rightleftarrows CO_3^{2} + 2H^+$	18.15 ± 0.06	Grenthe et al. (2020)
$CO_3^{2} + 2H^+ \rightleftarrows CO_2(aq) + H_2O$	16.68 ± 0.05	Grenthe et al. (2020)
$CO_3^{2} + H^+ \rightleftarrows HCO_3$	10.33 ± 0.05	Grenthe et al. (2020)
$UO_2^{2+} + H_2O \rightleftarrows UO_2(OH)^+ + H^+$	5.25 ± 0.24	Grenthe et al. (2020)
$UO_2^{2+} + 2H_2O \rightleftarrows UO_2(OH)_2(aq) + 2H^+$	12.15 ± 0.07	Grenthe et al. (2020)
$UO_2^{2+} + 3H_2O \rightleftarrows UO_2(OH)_3(aq) + 3H^+$	20.25 ± 0.42	Grenthe et al. (2020)
$UO_2^{2+} + 4H_2O \rightleftarrows UO_2(OH)_4^{2} (aq) + 4H^+$	32.40 ± 0.68	Grenthe et al. (2020)
$3\,UO_2^{2+} + 5H_2O \rightleftarrows (UO_2)_3(OH)_5^{+} + 5H^+$	15.55 ± 0.12	Grenthe et al. (2020)
$UO_2^{2+} + CO_3^{2} \rightleftarrows UO_2(CO_3)(aq)$	9.94 ± 0.03	Grenthe et al. (2020)
$UO_2^{2+} + 2CO_3^{2} \rightleftarrows UO_2(CO_3)_2^{2}$	16.61 ± 0.09	Grenthe et al. (2020)
$UO_2^{2+} + 3CO_3^{2} \rightleftarrows UO_2(CO_3)_3^{4}$	21.84 ± 0.04	Grenthe et al. (2020)
$2UO_2^{2+} + CO_2(g) + 4H_2O \rightleftarrows (UO_2)_2CO_3(OH)_3 + 5H^+$	19.01 ± 0.50	Grenthe et al. (2020)
$Ca^{2+} + UO_2(CO_3)_3^{4} \rightleftarrows CaUO_2(CO_3)_3^{2}$	5.36 ± 0.01	(Shang and Reiller, 2020) in NaCl
$2Ca^{2+} + UO_2(CO_3)_3^{4} \rightleftarrows Ca_2UO_2(CO_3)_3(aq)$	8.65 ± 0.02	(Shang and Reiller, 2020) in NaCl
$Si(OH)_4(aq) \rightleftarrows 2H^+ + SiO_2(OH)_2^{2}$	23.15 ± 0.09	Grenthe et al. (2020)
$Si(OH)_4(aq) \rightleftarrows H^+ + SiO(OH)_3$	9.80 ± 0.03	Grenthe et al. (2020)
$UO_2(OH)_3 + H_4SiO_4 \rightleftarrows UO_2(OH)_2SiO(OH)_3 + H_2O$	3.04 ± 0.34	p.w. measured at pH 9.2
	3.29 ± 0.26	p.w. measured at pH 10.5
	3.20 ± 0.21	p.w. average value of $\log_{10}K^{\circ}$ at pH 9.2 and 10.5
$UO_2(OH)_4^{2} + H_4SiO_4 \rightleftarrows UO_2(OH)_2SiO_2(OH)_2^{2} + H_2O$	3.21 ± 0.86	p.w. measured at pH 11.5
Reaction	$\log_{10} {}^{*}K_{s,0}^{\circ}$	Reference
$UO_3{:}2H_2O\ (cr) + 2H^+ = UO_2^{2+} + 3H_2O$	5.35 ± 0.13	(Altmaier et al., 2017; Grenthe et al., 2020)
$0.5Na_2U_2O_7{:}H_2O\ (cr) + 3H^+ = Na^+ + UO_2^{2+} + 2H_2O$	12.2 ± 0.2	(Altmaier et al., 2017; Grenthe et al., 2020)
Reaction	$\log_{10} \beta^{\circ}$	References
$UO_2^{2+} + H_4SiO_4 \rightleftarrows UO_2OSi(OH)_3^{+} + H^+$	0.06 ± 0.24	Lösch et al. (2020)
$UO_2^{2+} + 2H_2O + H_4SiO_4 \rightleftarrows UO_2(OH)_2SiO(OH)_3 + 3H^+$	17.05 ± 0.47	p.w.
	17.21 ± 1.09	Lösch (2020)
$UO_2^{2+} + 2H_2O + H_4SiO_4 \rightleftarrows UO_2(OH)_2SiO_2(OH)_2^{2} + 4H^+$	29.19 ± 1.10	p.w.

Table 2
Gibbs energies of formation for the main species used in this work.

Species	$\Delta_f G^{\circ}_m$ (kJ mol ^{1})	References
H_2O	237.140 ± 0.041	Grenthe et al. (2020)
UO_2^{2+}	952.551 ± 1.747	Grenthe et al. (2020)
$UO_2(OH)_3$	1548.384 ± 2.969	Grenthe et al. (2020)
$UO_2(OH)_4^{2}$	1716.171 ± 4.260	Grenthe et al. (2020)
$Si(OH)_4$ (aq)	1309.201 ± 1.017	Grenthe et al. (2020)
$UO_2OSi(OH)_3^{+}$	2251.021 ± 2.294	Grenthe et al. (2020)
$UO_2(OH)_2SiO(OH)_3$	2638.713 ± 3.568	p.w.
$UO_2(OH)_2SiO_2(OH)_2^{2}$	2806.557 ± 8.209	p.w.

geometries represented real minima, as they exhibited no imaginary frequencies.

The absolute energies of the electronic transitions involved in the luminescence of uranyl-hydroxide-silicate complexes. The CAM-B3LYP (Yanai et al., 2004) TD-DFT single-point calculations were carried out on spin-free excited-state structures. These calculations were performed with the Amsterdam Density Functional package (ADF, 2018.01, SCM, Theoretical Chemistry, Vrije Universiteit, Amsterdam, The Netherlands, http://www.scm.com). The spin-orbit coupling effects were considered using the ZORA Hamiltonian (van Lenthe et al., 1993). All atoms were described by TZ2P Slater-type basis sets (van Lenthe and Baerends, 2003) without freezing the atomic cores. The conductor-like screening COSMO model, implemented in ADF, was used to include the long-range effect of water solvent (Klamt and Schüürmann, 1993; Klamt, 1995; Klamt and Jonas, 1996).

3. Results and discussion

3.1. General spectral and temporal characteristics of U(VI)–OH–Si(OH)$_4$ complexes

In a first step, the stoichiometry of the uranyl hydroxide silicates species was derived on the basis of slope analysis of TRLFS spectroscopic data in combination with theoretical calculations – *vide post* for discussion. The nomenclature *pH 9.2-Complex, pH 10.5-Complex,* and *pH 11.5-Complex* is used to denote the complexes observed in solutions prepared at their respective designated pH values. It is important to note that at each pH, the potential coexistence of multiple complexes is plausible. The successive complexation of silicic acid with uranyl hydroxides is evident from the enhanced luminescent intensity and improved spectral profile after smoothing, as shown in Fig. 1. The raw spectra are shown in Fig. S2 of the SI. After normalizing the total area of the emission spectra in the presence of silicate, no significant changes were observed in peak positions with increasing silicate concentration.

Lorentzian-based peak separation analysis integrated in OriginPro software was applied to the decomposition of luminescence spectra acquired at $D = 20$ ns, as exemplified in Fig. 2 (see Table S1 of the SI for decomposition parameters). The selection of peak-shape model is dictated by the need to discern patterns in the shape and position of each peak, which corresponds to its unique energy signature. Three common models were tested in this work – Gauss, Gauss-Lorentz and Lorentz distributions. The Lorentz distribution function was found to provide slightly more accurate peak positions compared to the Gauss or Gauss-Lorentz models, resulting in a precise representation of the spectral bands. The advantage of the Lorentz distribution lies in its ability to capture the peak tailing often associated with asymmetric peaks because it represents a broader range of peak shapes with tails extending indefinitely (Di Marco and Bombi, 2001). The better fitting results with the Lorentz model suggest that the peaks in the U(VI)–OH–Si(OH)$_4$ spectra exhibit some level of asymmetry which is due to multiple coexisting species. In addition, the Loretz model is preferred to maintain consistency with the one used in computation. Characteristic peak maxima for *pH 9.2-Complex* were found at 506.75 ± 0.11, 528.66 ± 0.09, 551.19 ± 0.19 and 577.84 ± 0.45 nm, with uncertainties reported as 2σ. Similar principal peak properties were observed for the aqueous species at the other pH series, as detailed in Table 3.

Luminescence decay serves as a reliable indicator for discriminating and assigning different uranyl species based on their decay times in the investigated aqueous system. Through temporal decay analysis of the emission spectra, it is possible to draw specific conclusions and make

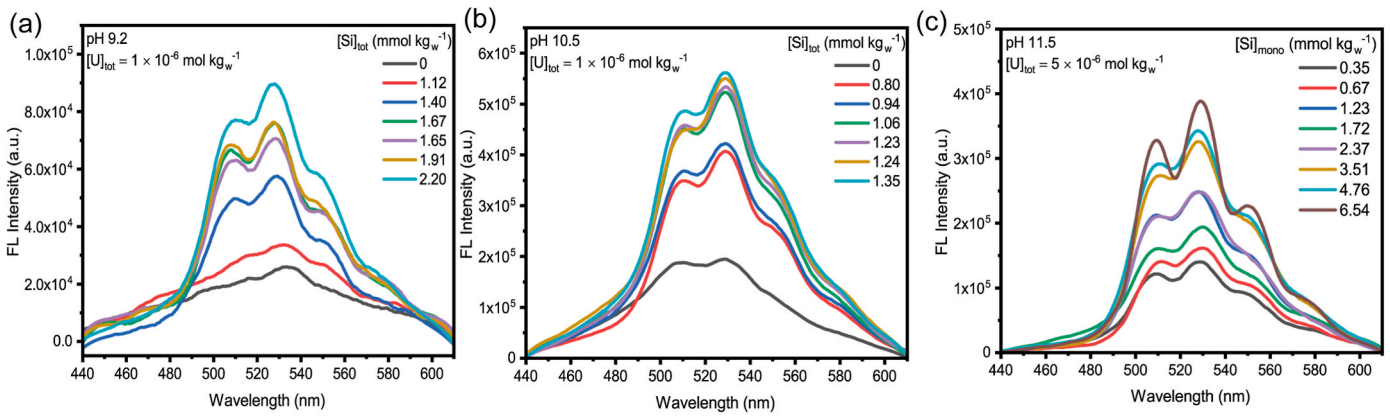

Fig. 1. Luminescence emission spectra of uranium(VI) at various [Si] at (a) pH 9.2, (b) pH 10.5 and (c) pH 11.5 and I_m 0.05 mol kg_w^{-1}. Initial delay time of D 20 ns and gate width W 0.5 ms, number of accumulation is 500. The spectra were smoothed using Savitzky-Golay method with Points of Window 100 and Polynominal Order 3.

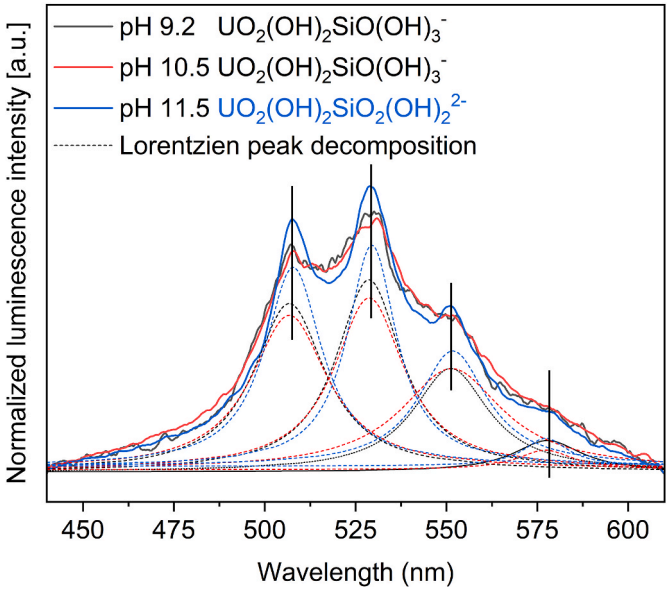

Fig. 2. Lorentzian peak decomposition of the measured luminescence spectrum of the samples at three pH values. $[U]_{tot}$ 1×10^{-6} mol kg_w^{-1}, $[Si]_{mono}$ 2.2×10^{-3} mol kg_w^{-1} at pH 9.2; $[U]_{tot}$ 1×10^{-6} mol kg_w^{-1}, $[Si]_{mono}$ 1.35×10^{-3} mol kg_w^{-1} at pH 10.5; $[U]_{tot}$ 5×10^{-6} mol kg_w^{-1}, $[Si]_{mono}$ 6.54×10^{-3} mol kg_w^{-1} at pH 11.5. The decomposition results are listed in Table S1 of the SI.

assignments regarding the formed emission species throughout the titration of silicic acid at various pH values. In this study, luminescence decay time analysis was conducted by acquiring the decay profiles as a function of delay time D, and subsequently fitting the integrated luminescence intensity to delay time using exponential functions. Three representative exponential fits at pH 9.2, 10.5 and 11.5 are presented in Fig. S3 of the SI. For the majority of uranyl silicate samples, an exponential decay can be adequately described with a single time constant, though at least two U(VI)–OH or U(VI)–OH–$Si(OH)_4$ complexes were expected to be present. The presence of two time constants in the mathematical fit can indicate the contribution of two chemically distinct species to the total luminescence or a slower ligand exchange compared to de-excitation rate. However, luminescence behavior cannot be easily concluded for such a complicated system containing hydroxo-uranyl and less well-known U(VI)–OH–$Si(OH)_4$ species. A very short decay time was observed using a double exponential decay function in several sample solutions and it was considered a spectral artefact in those cases. Moreover, the short decay time can be shorter than the step size of delay times in kinetic acquisitions, thereby reducing the mathematical significance of bi-exponential decay function. A mono-exponential fit was finally selected, taking into account both mathematical meaningfulness and the overall fit quality. Fig. 3 illustrates the decay time variations during silicic acid complexation at three pH values. A similar temporal trend can be observed in each measurement series, while the decay time of *pH 11.5-Complex* manifests a more pronounced increasing tendency compared to *pH 9.2-Complex* and *pH 10.5-Complex*. In Table 4 are gathered the comprehensive information on the concentrations of aqueous silicic acid and major luminescence parameters, i.e., intensity and decay time. The formation of *pH 9.2-Complex* and *pH 10.5-Complex*

Table 3
Position of the characteristic peaks of uranyl hydroxide silicates species at pH 10.5 and pH 11.5, compared with (synthetic) boltwoodite solid phases.

Phases	Peak positions					Reference
pH 9.2-Complex $UO_2(OH)_2SiO(OH)_3$		506.75 ± 0.11	528.66 ± 0.09	551.19 ± 0.19	577.84 ± 0.45 nm	p.w.
pH 10.5-Complex $UO_2(OH)_2SiO(OH)_3$		507.76 ± 0.12	529.94 ± 0.09	552.50 ± 0.22	578.83 ± 0.40	p.w.
pH 11.5-Complex $UO_2(OH)_2SiO_2(OH)_2^2$		507.82 ± 0.06	529.47 ± 0.06	551.73 ± 0.14	577.34 ± 0.34	p.w.
Synthetic boltwoodite		508	529	551		at 77 K (Vochten et al., 1997)
		~504.7	~526	~543.4	~567.2	[a](Arnold and Baumann, 2009)
		507.6	527.2	549.2		at 5.5 K (Ilton et al., 2006)
		505.86	526.86	549.15		Wang et al. (2005b)
	485.1	501.5	521.2	543	567.4	591.4 Arnold and Baumann (2009)
Boltwoodite		505.4	535.2	558.0	579.4	Wang et al. (2005b)

[a] Peak positions extracted from the luminescence spectrum published in (Vochten et al., 1997).

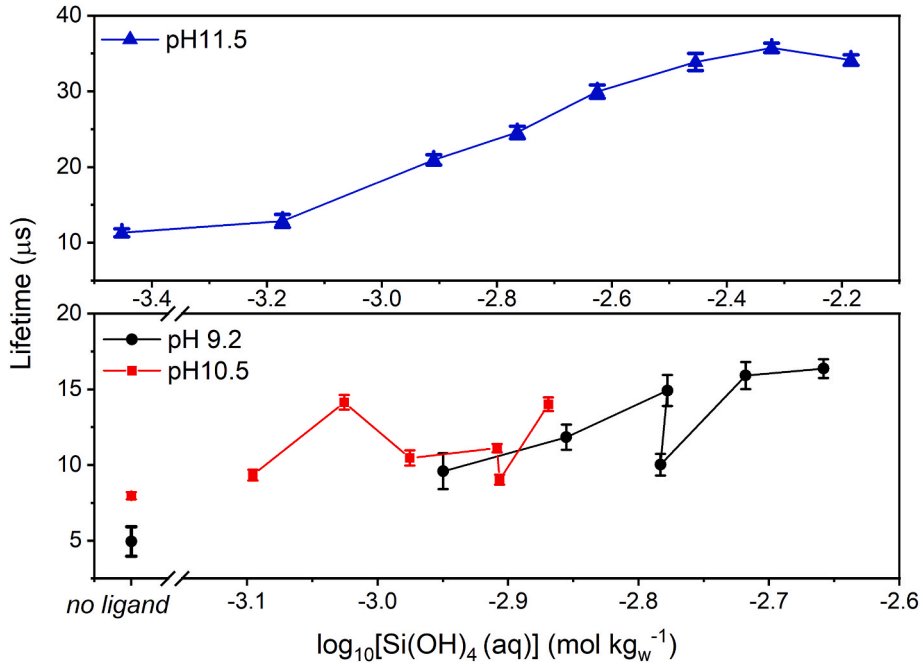

Fig. 3. Decay-times of the prepared sample solutions at three pH values. Exact values are listed in Table 4. The samples prepared in the absence of silicate at pH 9.2 and pH 10.5 are represented by pseudodata points.

exhibits slight fluctuations in the luminescence decay time within the studied $[Si]_{mono}$. At pH 9.2, the decay time increases from 9.59 ± 1.18 μs to 16.37 ± 0.62 μs during complexation, while a comparable fluctuating pattern of decay time is observed at pH 10.5, ranging from 9.34 ± 0.36 μs to 14.01 ± 0.45 μs. In contrast, at pH 11.5, even a minor concentration of silicic acid of 3.53×10^{-4} *m* gave a decay time of 11.31 ± 0.54 μs, comparable to that observed at slightly higher Si concentrations (1.2×10^{-3} *m* – 1.4×10^{-3} *m*) in the other two pH conditions. It is worth noting that the luminescence intensity and decay time stagnated with increasing $[Si]_{mono}$ from No. 6 of 3.51×10^{-3} M to No. 8 of 6.54×10^{-3} *m*, indicating the end of complexation.

The decay times of the studied complexes formed at the designed pH values were determined by averaging the τ values of the sample solutions presenting characteristics bands of uranyl hydroxides silicate species. It is observed that *pH 9.2-Complex* and *pH 10.5-Complex* exhibited a shorter decay time of 13.11 ± 2.20 μs and 11.35 ± 1.00 μs, compared with τ (*pH 11.5-Complex*) = 22.26 ± 2.05/25.43 ± 2.26 μs (averaged value of τ (No.1-6)/τ (No.1-8). The longer decay time of *pH 11.5-Complex* suggests the presence of a new complex different from *pH 9.2-Complex* and *pH 10.5-Complex*. In acidic conditions, Saito et al. (2015) reported a decay time of τ ($UO_2SiO(OH)_3^+$) = 13 ± 1 μs using TRLFS combined with parallel factor analysis. To the best of our knowledge, no other direct spectroscopic evidence or decay time data have been published for the formation of anionic uranyl hydroxide silicate species for comparison. Aqueous complexes can exhibit much shorter decay times than their solid minerals counterparts due to the presence of more surrounding quenchers, such as water molecules and a higher number of non-radiative energy transfers from the excited electrons to neighboring atoms. For example, $(Mg/Ca)_nUO_2(CO_3)_3^{(4-2n)-}$ complexes exhibit decay times in nanosecond range (Shang et al., 2020), while solid alkaline earth uranyl tricarbonates have decay times in the microsecond range (Amayri et al., 2005). In our study, the aqueous uranyl hydroxo silicates species showed longer decay times than the corresponding solid mineral – boltwoodite. Arnold and Baumann (2009) reported a lifetime of about 2.13 μs for pure boltwoodite, while Wang et al. (2005b) observed a bi-exponential decay behavior for natural and synthetic boltwoodite mineral species at room temperature, with decay times ranging from 0.9 to 7.4 μs.

Considering the effective charge of the uranyl ion as 3.3 ± 0.1, hexavalent UO_2^{2+} is restricted to accommodating more than four –OH ligands in its equatorial plane due to inter-ligand Coulomb repulsion and steric reasons (Fanghänel and Neck, 2002). The similarity observed in the complexation of uranyl ion by hydroxides and silicates may imply that the maximum coordination number of uranyl in $UO_2(OH)_xSiO(OH)_3^{1-x}$ or $UO_2(OH)_ySiO_2(OH)_2^{y}$ (x = 1, 2 or 3, y = 2 or 3) would also be four (Gorobets et al., 1977). The discussion on the stability of uranyl hydroxo silicates compounds with more than four hydroxides and silicate attachments will not be further elaborated through theoretical calculations.

3.2. *Theoretical luminescence spectra and structures*

The luminescence of U(VI) complexes arises from electronic transitions between excited and ground states coupled to vibronic progressions. The primary progression is dominated by the symmetrical stretching mode (υ_s) of the uranyl ion, with additional contribution from other vibrational mode mainly originating from the equatorial ligands in the coordination plane of uranyl moiety and by the vertical emission energy E_{VE}. The shape of luminescence spectra of U(VI) complexes is theoretically determined by their overall structural features and symmetries in both states, while the origin of the spectral envelope depends on the stoichiometry of the complex and the nature of equatorial ligands, particularly the acidity or basicity of the ligand. To establish a relationship between experimental luminescence spectra and specific chemical compounds, it is crucial to propose accurate structures for the relevant electronic states. In this computational study, multiple structures have been employed to deduce the correlation between theoretical predictions and experimental observations, ensuring a comprehensive analysis of the system.

To remain consistent with experimental knowledge regarding the potential chemical composition of species observed within the pH range from 9.2 to 11.5, we propose the following structures: $UO_2(OH)_2SiO(OH)_3$, $UO_2(OH)_2$-bid-$SiO(OH)_3$ and $UO_2(OH)_2SiO_2(OH)_2^{2-}$. For simplicity, we will refer to these complexes as *Structure A*, *Structure B*, *Structure C*, respectively. As depicted in Fig. 4, the geometrical structures of these conformers are proposed based on chemical reasoning. Other

Table 4
Values of $[Si]_{mono}$ corrected by molybdate determination and luminescence intensity at delay time of 20 ns and decay time measured for each sample solution.

pH 9.2	$[Si]_{mono}$ (mol kg_w^{-1}) corrected by monomeric proportion	Luminescence Intensity at D = 20 ns [a]	Decay time τ (μs)
No. 1	0	2.42×10^6 ($\pm 1.42 \times 10^5$)	4.94 ± 0.97
No. 2	1.12×10^{-3}	3.09×10^6 ($\pm 4.80 \times 10^5$)	9.59 ± 1.18
No. 3	1.40×10^{-3}	3.78×10^6 ($\pm 2.04 \times 10^5$)	11.84 ± 0.83
No. 4	1.67×10^{-3}	5.12×10^6 ($\pm 1.78 \times 10^5$)	14.92 ± 1.02
No. 5	1.65×10^{-3}	5.08×10^6 ($\pm 2.97 \times 10^5$)	10.02 ± 0.72
No. 6	1.91×10^{-3}	5.25×10^6 ($\pm 2.18 \times 10^5$)	15.92 ± 0.90
No. 7	2.20×10^{-3}	5.94×10^6 ($\pm 1.77 \times 10^5$)	16.37 ± 0.62
pH 10.5			
No. 1	0	1.59×10^7 ($\pm 4.98 \times 10^5$)	3.98 ± 0.23
No. 2	8.02×10^{-4}	2.73×10^7 ($\pm 8.16 \times 10^5$)	9.34 ± 0.36
No. 3	9.43×10^{-4}	2.95×10^7 ($\pm 1.03 \times 10^6$)	14.14 ± 0.49
No. 4	1.06×10^{-3}	3.50×10^7 ($\pm 1.57 \times 10^6$)	10.47 ± 0.51
No. 5	1.23×10^{-3}	3.62×10^7 ($\pm 9.10 \times 10^5$)	11.12 ± 0.27
No. 6	1.24×10^{-3}	3.79×10^7 ($\pm 1.10 \times 10^6$)	9.03 ± 0.32
No. 7	1.35×10^{-3}	3.87×10^7 ($\pm 1.27 \times 10^6$)	14.01 ± 0.45
pH 11.5			
No. 1	3.53×10^{-4}	9.16×10^6 ($\pm 3.00 \times 10^5$)	11.31 ± 0.54
No. 2	6.71×10^{-4}	1.02×10^7 ($\pm 3.84 \times 10^5$)	12.86 ± 0.87
No. 3	1.23×10^{-3}	1.54×10^7 ($\pm 3.10 \times 10^5$)	20.95 ± 0.67
No. 4	1.72×10^{-3}	1.32×10^7 ($\pm 3.51 \times 10^5$)	24.58 ± 0.81
No. 5	2.37×10^{-3}	1.55×10^7 ($\pm 4.13 \times 10^5$)	29.95 ± 0.88
No. 6	3.51×10^{-3}	1.98×10^7 ($\pm 4.55 \times 10^5$)	33.88 ± 1.13
No. 7	4.76×10^{-3}	2.11×10^7 ($\pm 2.62 \times 10^6$)	35.73 ± 0.62
No. 8	6.54×10^{-3}	2.13×10^7 ($\pm 4.51 \times 10^5$)	34.14 ± 0.71

[a] The uncertainties associated with the value of FI (D 20ns) calculated by a simple trapezoidal method, were determined from the mono-exponential fits of luminescence intensity decay giving the values of FI (D 0 ns) and decay time τ (μs).

candidate structures are also discussed in the following section but are ruled out due to thermodynamic and theoretical considerations (*vide post*). *Structures A* and *B* share identical chemical compositions but differ in their silicate binding modes, specifically between a monodentate and bidentate mode, respectively. The energy difference between these two conformers has been computed to be only 5.9 kJ/mol at PBE0 level of theory. In contrast, *Structures B* and *C* hold the same coordination mode, involving silicic acids with varying degrees of deprotonation. The structural differences are essential to understand their theoretical luminescence spectra. While there are no literature data on the structural parameters of aqueous uranyl hydroxo silicate complexes for direct validation, the correctness of our theoretical structures is supported by previous successful use of DFT with PBE0 applied to the description of uranium(VI) complexes (Tecmer et al., 2012; Oher et al., 2023).

Table 5 reports the key bond distances of the excited-state *Structures A-C* and compares them to the bond lengths determined in their ground states. Overall, the behavior of bond distances is similar in both states. The variations in bond lengths in the excited state, resulting from changes in coordination mode and deprotonation degree of silicic acid, are of a similar magnitude like those observed in the ground state. Specifically, in the ground state, the U-O_{yl} bond lengths of the complexes falls within the range from 1.780 to 1.807 Å. The U-OH bond lengths range from 2.177 to 2.245 Å and the U-O_{eq} bond lengths range from 2.224 to 2.343 Å. Looking at the available geometrical parameters obtained in both states, it can be concluded that the U-O_{yl} and U-OH are more sensitive with respect to the structural symmetry rather than the coordination number in the inner sphere of uranyl ion, as evidenced by the comparable bond lengths in *Structures A* and *B* but elongated bond lengths in the more symmetrical *Structure C* with doubly deprotonated silicic acid. Such observation justifies the tendency in the U-O_{yl} symmetrical stretching vibrational frequencies υ_s, as listed in Table 5. It was inferred that a stronger basicity of ligands in ionic interaction with uranyl moiety can result in a larger decrease of the symmetrical stretching frequency (Wang et al., 2008). This explanation holds for $SiO_2(OH)_2^{2-}$ in *Structure C*, which is a stronger base than $SiO(OH)_3^-$ in *Structures A* and *B* in terms of intrinsic complexation strength dictated by charge (Parr and Pearson, 1983).

Moreover, one should point that the U-O_{yl} bond length is not equally symmetrical in *Structures A* and *B* compared to *Structure C*. Previous research has shown that molecules with higher symmetry tend to exhibit larger quantum yield as well as longer decay-time due to the presence of symmetry-forbidden transitions, as evidenced by examining the experimental luminescence parameters of a series of organic molecules (Nizhegorodov, 1992). In the case of *Structure C*, the electron redistribution upon complexation of $SiO_2(OH)_2^{2-}$ with uranyl hydroxides results in a more symmetric structure compared to *Structures A* and *B*, where $SiO(OH)_3^-$ is complexed with uranyl hydroxides. The enhanced symmetry in *Structure C* leads to a reduction in nonradiative pathways, theoretically resulting in less energy losses between the excitation and emission processes thus leading to a longer decay-time. This finding provides significant evidence to support the designation of *Structure C* as the species with longer decay-time observed in this work at pH 11.5,

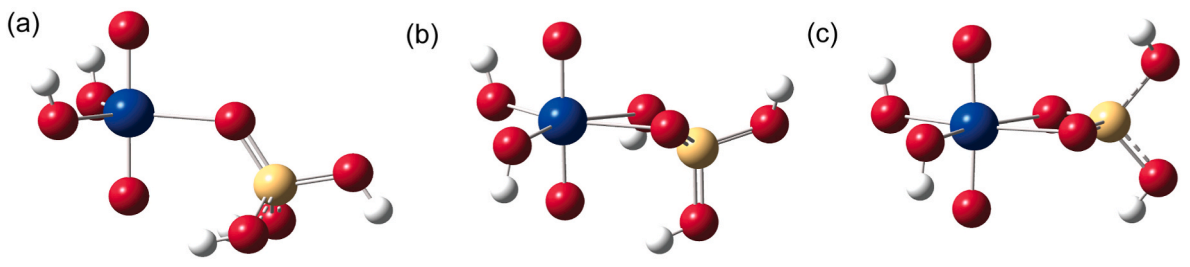

Fig. 4. A graphical representation of the geometrical theoretical models of uranium(VI) silicate complexes obtained at the R-DFT/PBE0 level of theory. A – $UO_2(OH)_2SiO(OH)_3^-$, B – $UO_2(OH)_2$-bid-$SiO(OH)_3^-$, C – $UO_2(OH)_2SiO_2(OH)_2^{2-}$.

Table 5
Ground and luminescent state geometries (in Å) and symmetrical uranyl stretching frequency (υ_s) of uranium(VI) hydroxo silicate complexes obtained with relativistic DFT and TD-DFT methods respectively using the PBE0 functional of density.

	$U\text{-}O_{yl}$	U-OH	$U\text{-}O_{eq}$[a]	υ_s (cm^{-1})
Ground state				
$A\text{-}UO_2(OH)_2SiO(OH)_3$	1.783/1.798	2.177	2.224	836
$B\text{-}UO_2(OH)_2\text{-bid-}SiO(OH)_3$	1.780/1.800	2.179	2.322	838
$C\text{-}UO_2(OH)_2SiO_2(OH)_2^2$	1.807	2.245	2.343	811
Luminescent state				
$A\text{-}UO_2(OH)_2SiO(OH)_3$	1.810/1.836	2.167	2.243	753
	+ 0.027/0.038[b]	*0.01*[b]	*+ 0.019*[b]	*83*[c]
$B\text{-}UO_2(OH)_2\text{-bid-}SiO(OH)_3$	1.817/1.830	2.170	2.324	763
	+ 0.037/0.03[b]	*0.009*[b]	*+ 0.002*[b]	*75*[c]
$C\text{-}UO_2(OH)_2SiO_2(OH)_2^2$	1.845	2.256	2.353	727
	+ 0.038[b]	*+ 0.011*[b]	*+ 0.01*[b]	*84*[c]

[a] Average value of $r(U\text{-}O_{eq})$ in Structures B and C where more than one oxygen in the equatorial plane of uranium is attached to Si.
[b] Elongation (+) or shortening (−) of bond lengths in the excited state compared to their values in the ground state.
[c] $\Delta\upsilon_s \quad \upsilon_{s,ground\ state} - \upsilon_{s,excited\ state}$ (cm^{-1}).

despite the computationally obtained spectrum using the Lorentzian convolution not precisely matching the experimentally measured one (*vide post*).

Upon excitation of *Structures A-C*, it is observed that the $U\text{-}O_{yl}$ and $U\text{-}O_{eq}$ bond lengths undergo elongation within the range of 0.002–0.038 Å. Notably, the $U\text{-}O_{yl}$ bond displacement exhibits a more pronounced sensitivity to excitation, with an elongation of approximately 0.030 Å. This displacement is attributed to the ligand-to-metal charge transfer (LMCT), with a larger contribution from the axial oxygen atoms, resulting in a larger displacement of the $U\text{-}O_{yl}$ bond distance. Similar structural behavior during the transition from the luminescent to ground state has been observed in the previous theoretical studies (Su et al., 2011, 2014; Oher et al., 2020a). Additionally, an average of U-OH and $U\text{-}O_{eq}$ geometrical displacement in equatorial ligand field is found to be within the range of 0.002–0.019 Å. More specifically, the U-OH bond is shortened by approximately 0.010 Å in *Structures A* and *B* but extended by a similar length in *Structure C*. In comparison, the $U\text{-}O_{eq}$ bond length remains essentially unchanged in *Structure B* during the transition to the luminescent state, while it is elongated by 0.019 and 0.010 Å in *Structures A* and *B*, respectively.

On the other hand, the uranyl symmetrical stretching frequencies are separately calculated for both states because of their relevance for the luminescence intensity distribution of U(VI)-based complexes. In the U(VI)–OH–$Si(OH)_4$ complexes, the vibronic progressions begin at the peak of the lowest energy, characterized by E_{VE} and continue with a band spacing primarily determined by the ground-state υ_s value. The emission process in the studied complexes corresponds to a local transition from one of the non-bonding to bonding uranyl orbitals, with a moderate metal-to-ligand charge transfer character. In this work, the vertical emission energy E_{VE} was determined at TD-DFT/CAM-B3LYP calculations, including the long-range effect of water solvent with the COSMO model. The theoretical values of E_{VE} and υ_s together with the experimentally measured peak positions are shown in Table 6. In the ground state, the values of υ_s are determined as 836, 838 and 811 cm^{-1} for *Structures A*, *B* and *C*, respectively, while their excited-state values are found to be lower by about 80 cm^{-1}. Since this vibrational mode is coupled to the electron transitions observed in the luminescence of U(VI) complexes, the theoretical band spacing can be compared to the experimentally measured values. When examining Table 6 and it becomes evident that the averaged band spacing values obtained from the experimental data show a remarkable similarity between the U(VI)–OH–$Si(OH)_4$ complexes at pH 9.2 and 10.5, while exhibiting a noticeable shift towards lower vibrational energies of 16–19 cm^{-1} for the complexes at pH 11.5. A similar trend is observed in the averaged ground-state theoretical values of υ_s: *Structures A* and *B*, which possess a lower degree of symmetry, exhibit higher values of υ_s, while *Structure C*, with its enhanced symmetry, undergoes a significant decrease in υ_s by approximately 25–27 cm^{-1}. Moreover, the experimental values of the vertical emission energies E_{VE} in *Structures A-C* are in good agreement with the experimental luminescence origin, within the accuracy of calculations (±10 nm), and the biggest discrepancy is observed to be around 8 nm. With the values of E_{VE} and υ_s, it is possible to computationally generate the theoretical luminescence spectra of *Structures A-C*, enabling us to infer the potential chemical composition of U(VI)–OH–Si$(OH)_4$ complexes under different conditions.

Fig. 5 exemplifies the comparison between experimental and computed spectra without first peak adjustment, see Table 6 for computed peak values (see Fig. S4 for comparison with the first peak in the computed spectra shifted to align with the experimental spectra). The theoretical luminescence spectrum of *Structure C* shows a noticeable deviation from the experimental pattern, whereas *Structures A* and *B* exhibit good agreement. Such discrepancies can be attributed to the higher symmetry of *Structure C*, which causes certain ligand motions to be degenerate, resulting in reduced coupling with uranyl symmetrical

Table 6
Theoretical (TD-DFT/CAM-B3LYP) and experimental spectra characteristics of uranium(VI) silicate complexes. E_{VE} corresponds to the vertical emission energy in *nm*. The experimental υ_s value is deduced by Lorentzian fitting procedure.

Complex	spectral maximum (nm)				
	E_{VE}	$E_{VE} + 1\upsilon_s$	$E_{VE} + 2\upsilon_s$	$E_{VE} + 3\upsilon_s$	υ_s (cm^{-1})
Experimental Values					
[a] TRLFS spectrum at pH 9.2	506.75	528.66	551.19	577.84	809
[a] TRLFS spectrum at pH 10.5	507.76	529.94	552.50	578.83	806
[a] TRLFS spectrum at pH 11.5	507.82	529.47	551.73	577.34	790
Theoretical Values					
$A\text{-}UO_2(OH)_2SiO(OH)_3$	507.64	530.14	554.72	581.70	836
$B\text{-}UO_2(OH)_2\text{-bid-}SiO(OH)_3$	510.80	533.65	558.63	586.06	838
$C\text{-}UO_2(OH)_2SiO_2(OH)_2^2$	498.53	519.53	542.39	567.34	811

[a] refer to Fig. 2.

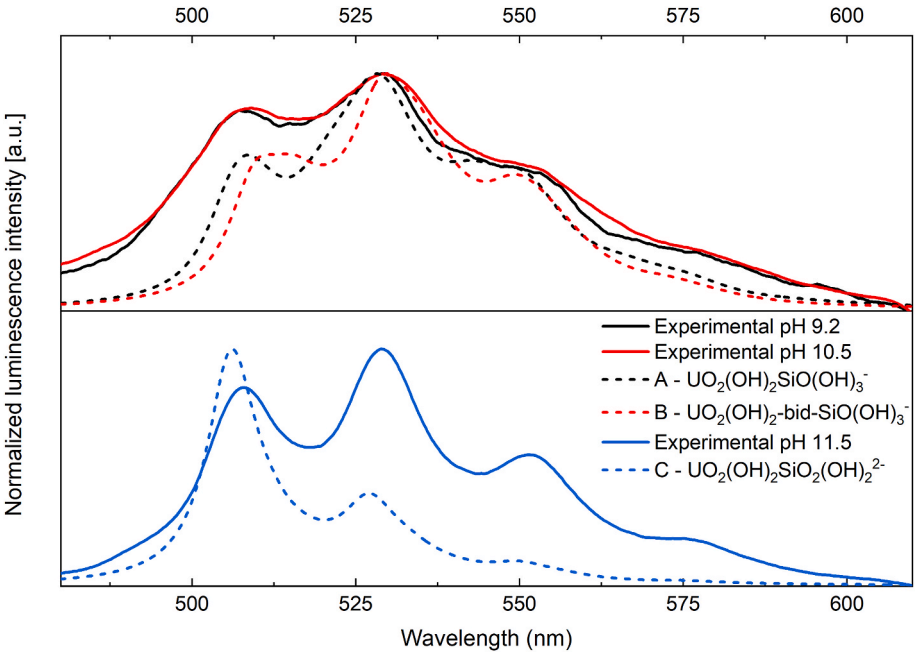

Fig. 5. Comparison of experimental data normalized by maximum intensity to expected theoretical models.

stretching mode and intense oscillator strength of the first band. Consequently, the band spacing in the spectrum of *Structure C* appears broader compared to *Structures A* and *B*. Moreover, the slightly hypsochromic shift observed in the computed spectrum of *Structure C* provides further evidence of less energy losses during the emission process, which is inherently determined by its higher symmetry (Lakowicz, 2006).

Previous comparison of luminescence emission spectra and decay times between the species at pH 9.2 and 10.5 revealed remarkable similarities, as evidenced by their nearly identical fingerprint profiles. The closely matched spectral features and temporal properties further support the notion that the luminescence properties of these species at pH 9.2 and 10.5 are deeply linked, most possibly arising from similar coordination environments or structural arrangements. Considering the prevalence of mono-deprotonated silicic acid under these conditions, the resulting structures are naturally attributed to either *Structure A* or *B*. However, it is worth noting that the coordination number of three in the inner sphere of uranyl ion is rarely observed in U(VI) complexes because of their chemically unstable properties. We lean towards a higher likelihood that the species in question correspond to *Structure B*. This assumption serves as a basis for further discussion and analysis.

3.3. Evaluation of equilibrium constants

Thermodynamic modelling using the uranium(VI) hydrolysis formation constants in Table 1 predicted that in the absence of silicate, $UO_2(OH)_3$ is the dominating species at pH 9.2 and it remains as the main species at pH 10.5. At pH 11.5, the non-luminescent $UO_2(OH)_4^{2}$ becomes the main species. Eq. (3) and Eq. (4) represent the formation reactions of $UO_2(OH)_2SiO(OH)_3$ and $UO_2(OH)_2SiO_2(OH)_2^{2}$, starting respectively from $UO_2(OH)_3$ (pH 9.2 and 10.5) and $UO_2(OH)_4^{2}$ (pH 11.5) according to the preliminary calculations. The resulting species of different conformations and compositions are exemplified in Eq. S1 and Eq. S2 of the SI.

$$UO_2(OH)_3 + Si(OH)_4(aq) = UO_2(OH)_2SiO(OH)_3 + H_2O(l)$$

$$K'_{1,3,2,1} = \frac{[UO_2(OH)_2SiO(OH)_3^-]}{[UO_2(OH)_3^-][Si(OH)_4(aq)]} \quad \text{Eq. 3}$$

$$UO_2(OH)_4^{2} + Si(OH)_4(aq) = UO_2(OH)_2SiO_2(OH)_2^{2} + 2H_2O(l)$$

$$K'_{1,4,2,2} = \frac{[UO_2(OH)_2SiO_2(OH)_2^{2-}]}{[UO_2(OH)_4^{2-}][Si(OH)_4(aq)]} \quad \text{Eq. 4}$$

where squared brackets represent concentration on molality scale (mol kg_w^{-1}). $K'_{m,n,q,l.}$ refers to the formation constant of the reaction with *m*: number of uranium, *n*: number of –OH in the predominant uranyl hydroxo species in the absence of silicic acid, *q*: number of –OH attached to uranium atom and *l*: degree of deprotonation of silicic acid. For a thorough description of the formation of $UO_2(OH)_xSiO(OH)_3^{1\ x}$ or $UO_2(OH)_ySiO_2(OH)_2^{\ y}$ (x = 1, 2 or 3, y = 2 or 3) species, the formation equations for $K'_{1,3,3,1}$ and $K'_{1,4,1,2}$ are listed in the SI (*see* Eq. S2 and Eq. S3 of the SI). For simplification, $K'_{1,3,2,1}$ and $K'_{1,4,2,2}$ are written as $K'_{1,3,1}$ and $K'_{1,4,2}$ in the main text. The formation of U(VI)–OH-$(Si(OH)_4)_n$ polymeric silicic acid complexes, e.g., $UO_2(OH)_2[SiO(OH)_3^-]_n^n$ and $UO_2(OH)_2[SiO_2(OH)_2]_n^{2n}$, are equally described in the SI (*see* Eq. S4 to Eq. S7 of the SI).

The complexation number of silicic acid is estimated by the slope analysis, which establishes a linear relationship between the logarithm of relative concentration ratio *R* between U(VI)–OH–$Si(OH)_4$ and U(VI)-OH complexes *versus* $\log_{10}[Si(OH)_4(aq)]$. The degree of complexation is examined by the variation of luminescence intensity proportional to the formed uranyl hydroxides silicates species as a function of the concentration of monomeric silicic acid, which was determined by the photometric molybdate method (*vide infra*). The [Si] concentrations were restricted to low values with $[Si]_{mono}$ of at least > 90 %, ensuring minor complexation of U(VI) with polysilicates. At pH 9.2 and 10.5, the luminescence spectra of the sample solutions in the absence of silicic acid (No. 0 in Table 4) exhibit comparable peak positions and decay times to the literature data of $UO_2(OH)_3$ (Drobot et al., 2015, Drobot et al., 2016). As shown in Eq. (5), the slope value *n* represents the stoichiometric number of silicic acid involved, and the intercept $\log_{10}K'$ is assigned to the stepwise equilibrium constant at $I_m = 0.05$ *m*.

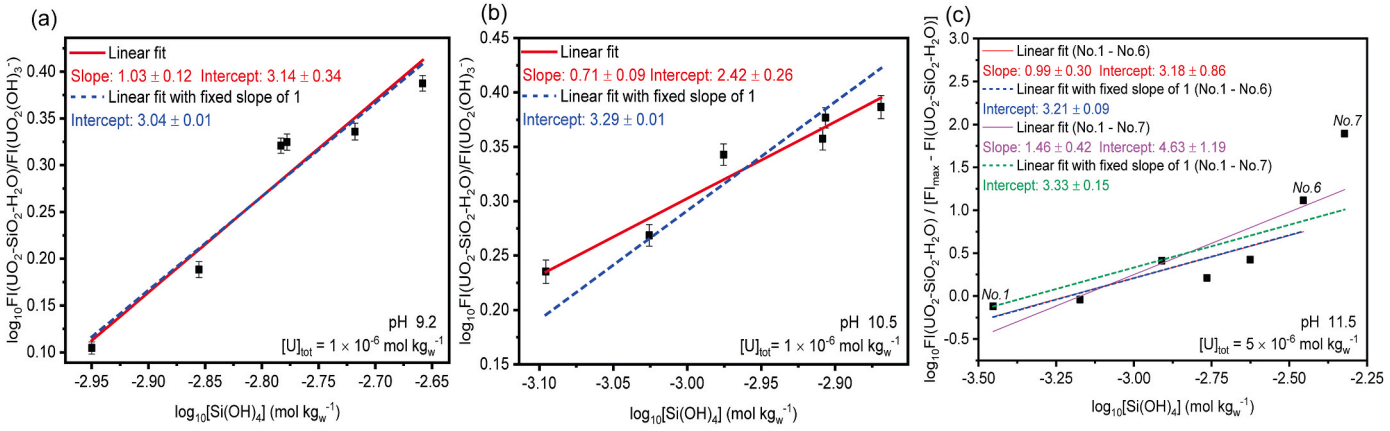

Fig. 6. Plots of logarithmic luminescence intensity ratio as a function of $\log_{10}[Si(OH)_4\ (aq)]$ at (a) pH 9.2, (b) pH 10.5 and (c) pH 11.5.

$$\log_{10}R = \log_{10}\frac{[UO_2(OH)_2SiO(OH)_3^-]}{[UO_2(OH)_3^-]} = \log_{10}\frac{FI\ (UO_2(OH)_2SiO(OH)_3^-)}{FI\ (UO_2(OH)_3^-)} = \log_{10}K'_{1,3,1} + n\ \log_{10}[Si(OH)_4(aq)] \quad \text{Eq. 5}$$

where the nominator represents the luminescence intensity at $D = 20$ ns of uranyl hydroxides silicate species and the denominator is that of $UO_2(OH)_3$ – the dominant species at pH 9.2 and 10.5. Due to the absence of luminescence of $UO_2(OH)_4^{2-}$ species at room temperature (Martínez-Torrents et al., 2013), the concentration ratio R was described in Eq. (6) for the series at pH 11.5.

$$\log_{10}R = \log_{10}\frac{FI\ (UO_2(OH)_2SiO_2(OH)_2^{2-})}{FI\ (UO_2(OH)_4^{2-})} = \log_{10}\frac{FI\ (UO_2(OH)_2SiO_2(OH)_2^{2-})}{FI_{max} - FI\ (UO_2(OH)_2SiO_2(OH)_2^{2-})} = \log_{10}K'_{1,4,2} + n\ \log_{10}[Si(OH)_4(aq)] \quad \text{Eq. 6}$$

where FI_{max} denotes the maximum luminescence intensity of U(VI)–OH–Si(OH)$_4$ species in the course of titration, assuming the complete complexation of uranyl hydroxides with silicic acid. The $FI = 2.13 \times 10^7$ of No.8 was assigned to FI_{max} as the samples No.6-No.8 showed stagnated intensity and lifetime with increasing silicate concentration (see Table 4).

Experimental data in logarithmic scale were fitted to linear relationship by a weighted least-square regression. The uncertainties of each experimental point are estimated from the *FI* integration, as shown in Fig. 6. The slope of *ca.* 1 obtained at pH 9.2 and 10.5 provides strong evidence for the complexation of uranyl hydroxides with monomeric silicate. Rounding off the slope values to the nearest integer of one results in the conditional equilibrium constants $\log_{10}K'_{1,3,1} = (3.04 \pm 0.01)$ at pH 9.2, which slightly deviates from the values obtained from simple linear regression, i.e. $\log_{10}K'_{1,3,1} = (3.14 \pm 0.34)$. In terms of uncertainties, the estimates of $\log_{10}K'_{1,3,1}$ and $\log_{10}K'_{1,4,2}$ obtained through slope-restricted least squares regression are chemically unrealistic because the standard deviations of regression coefficients in simple linear fits are calculated based on covariance matrices of experimentally measured variables, whereas no covariance can be generated between slope and intercept with slope fixation. The uncertainties assigned to the stepwise formation constants $\log_{10}K'$ were retained identical to the ones from simple linear regression in further analysis. The conditional equilibrium constants were extrapolated to infinite dilution with activity coefficients evaluated by the Davies equation (Davies, 1962), which is generally accepted for ionic strengths below 0.1 *m* in the NEA-TDB guidelines (Wanner and Östhols, 1999). The activity coefficient γ_i of the participating ion *i* charged z_i at the ionic strength I_m in the molal scale and 25 °C were calculated using the equation as follows:

$$\log_{10}\gamma_i = Az_i^2\left(\frac{\sqrt{I_m}}{1+\sqrt{I_m}} - 0.3I_m\right) \quad \text{Eq. 7}$$

where A = 0.5102–the temperature dependent Debye-Huckel constant. The value of 0.3 is an estimated value considering size effects and electronic density distribution factors.

Table 1 lists the binding constants of silicic acid to uranyl hydroxide species at infinite dilution. The plots at pH 9.2 and 10.5 both exhibited a linear correlation with respective slope values of (1.03 ± 0.12) and (0.71 ± 0.09) throughout the complexation of Si. The comparable $\log_{10}K_{1,3,1}^\circ$ values determined at these two pH values ruled out the possibility of previously proposed candidates – $UO_2(OH)SiO(OH)_3(aq)$ and $UO_2(OH)_3SiO(OH)_3^{2-}$. As illustrated in Eq. S1 and Eq. S2 of the SI, the titration at pH 9.2 and 10.5 would result in a difference in $\log_{10}K_{1,3,1}^\circ$ of approximately one order of magnitude because their formation reactions involve a dependence on actual pH values. On the other hand, their theoretically computed spectra are systematically inaccurate due to the unrealistic coordination in the first sphere of uranyl ion (*not shown*).

The average value of $\log_{10}K_{1,3,1}^\circ$ obtained at pH 9.2 and 10.5 was assigned to the stepwise formation constant of $UO_2(OH)_2SiO(OH)_3$. The cumulative equilibrium constants $\log_{10}\beta_{1,3,1}^\circ$ were derived with NEA-selected $\log_{10}\beta^\circ(UO_2(OH)_3^-)$ and $\log_{10}\beta^\circ(UO_2(OH)_4^{2-})$, as shown in Table 1. The value of $\log_{10}\beta_{1,3,1}^\circ(UO_2(OH)_2SiO(OH)_3^-) = -(17.05 \pm 0.47)$ determined in the present work agrees within the uncertainties with the literature value of $\log_{10}\beta_{1,3,1}^\circ = -(17.21 \pm 1.09)$ determined by means of sorption experiments (Lösch, 2020). At pH 11.5, a satisfactory linear relationship was obtained from the fit of the Samples No.1-No.6, resulting in a slope value of (0.99 ± 0.30) with $\log_{10}K_{1,4,2}^\circ = (3.18 \pm 0.86)$, while the fixed-slope analysis gave $\log_{10}K_{1,4,2}^\circ = (3.21 \pm 0.09)$. In contrast, a moderate linear relationship including the Sample No.7 yielded a slope value of (1.46 ± 0.42) and large uncertainties in the intercept with $\log_{10}K_{1,4,2}^\circ = (4.63 \pm 1.19)$ and (3.33 ± 0.15) for fits with slope set free and fixed, respectively.

The present results challenge the assumption that silicate monomers are the sole species at low concentrations. Our molybdate results indicate polymerization even for undersaturation conditions of silicic acid. For instance, the monosilicate percentage varies from 93.85 % to 89.89 % in the Sample No.6 to No.8. This is in agreement with the findings of Lösch et al. (2020) using the electrospray-ionization mass spectrometry (ESI-MS) to identify the polyciliate at acidic conditions below the limits of silicic acid solubility. Indeed, both monomeric and dimeric silica are susceptible to react with the ammonium molybdate in the colorimetric procedure (Tanaka and Takahashi, 2001). The absence of polymeric

silica cannot be simply predicted from the theoretical mononuclear limit, one has to acknowledge the difficulties in defining a boundary [Si] concentration in which a change of single practical factor, e.g., waiting time of reactions, can develop a network of polymerized $[SiO_4]^4$ in solution. The formation of negatively mono-charged (SiO)(SiOH)$_{m\text{-}1}$ and double-charged (SiO)(SiOH)$^2_{m\text{-}2}$ polymeric molecule of silicic acid under alkaline conditions may *a fortiori* lead to an underestimation of the formation constants of monomeric U(VI) hydroxides silicates species. Furthermore, it remains speculative whether polymeric silicic acids interact more strongly with uranyl ion compared to monomers (Jensenf and Choppin, 1996; Yusov and Fedoseev, 2005). In the present study, the formation of minor U(VI)–OH-polymeric silicic acid species may be possible in the final samples within the series of pH 11.5, as reflected by the slope value of (1.46 ± 0.42) in the slope analysis for the Samples No.1-No.7. On the other hand, FI (No.7) = 2.11 × 10^7 closely mirrors the intensity value of No.8 (FI = 2.13 × 10^7), leading to an overemphasis on this single point in the slope calculation and contributing a disproportionately large $\log_{10}R$ in Eq. (6), which drives the slope value from (0.99 ± 0.30) to (1.46 ± 0.42). The small difference in terms of luminescence intensity between No.7 and No.8 has an outsized impact on the slope calculation. Therefore, the Sample No. 7 at pH 11.5 was excluded from the slope analysis with FI_{max} = FI (No.8). The results of the slope analysis for the Samples No.1-No.6 with FI_{max} = FI (No.8) suggest that the experimental methodology is adequate within the range of measurement and calculation errors. In the course of [Si] complexation, one can observe the largely impeded presence of U(VI)-OH due to the formation of U(VI)–OH–Si(OH)$_4$ species. Moreover, the spectral characteristics of the latter were not impacted regardless of possible moderate polymerization of Si(OH)$_4$ at pH 11.5. A detailed discussion on the robustness of this approach is provided in the Supporting Information (Fig. S5 and related text).

The proportions of uranyl hydroxides silicates complexes in the prepared samples were calculated with the determined equilibrium constants, as shown in Fig. S6. The dominant species at pH 9.2 – $UO_2(OH)_2SiO(OH)_3$ – increased from 48% to 65% in the course of complexation. However, at pH 10.5, the primary and secondary dominant species were respectively $UO_2(OH)_3$ and $UO_2(OH)^2_4$, and the fraction of monomeric $UO_2(OH)_2SiO(OH)_3$ varied from 11% to 16%. At pH 11.5, the fraction of $UO_2(OH)_2SiO_2(OH)^2_2$ remained below 15% and the non-luminescent $UO_2(OH)^2_4$ dominated the sample solutions during complexation. The speciation profiles reflect the difficulties in probing the interplay between uranium and monomeric silicic acid under alkaline conditions without interference of polymeric silicic acid. Nonetheless, the strong luminescent signal and longer lifetime observed for uranyl hydroxides silicates, in comparison to uranyl hydroxides complexes, serve as compensatory factors that mitigate these challenges. Based on the luminescence spectra, no obvious changes in spectral peak positions were observed for a transition from $UO_2(OH)_2SiO(OH)_3$ to $UO_2(OH)_2SiO_2(OH)^2_2$. The consistency in the uranium inner-sphere structure, as revealed by theoretical calculations, supports this observation. The spectral peak information can serve as a fingerprint, enabling the identification of bidentate coordination of silicate with the uranyl moiety. Furthermore, the increased lifetime of $UO_2(OH)_2SiO_2(OH)^2_2$ compared to that of $UO_2(OH)_2SiO(OH)_3$ seems indicate an enhanced quenching effects of H_3SiO_4 compared to $H_2SiO^2_4$, which may be attribute to the more symmetric structure of the latter.

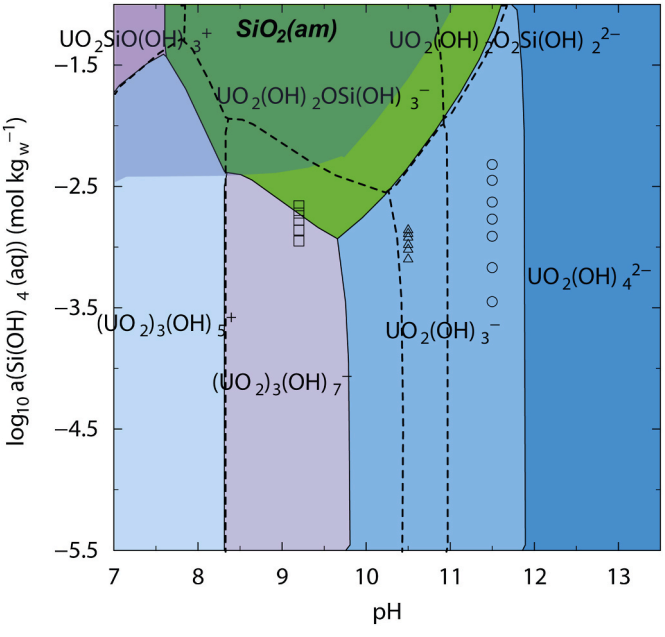

Fig. 7. Predominance plots of U(VI)–OH–Si(OH)$_4$ system in 0.05 mol kg_w^{-1} $NaNO_3$ at $C(U)_{tot}$ 10^{-7} mol kg_w^{-1} using thermodynamic data reported in the NEA-TDB (colored area) and by Altmaier et al. (Altmaier et al., 2017) (dashed lines) for U(VI) hydrolysis and stability constants for U(VI)–OH–Si(OH)$_4$ complexes as determined in this work. Experimental points at pH 9.2, 10.5 and 11.5 are shown with squares, triangles and circles, respectively.

Fig. 7 the predominance diagram of U(VI)–OH–Si(OH)$_4$ system constructed with NEA-TDB data selection complemented with the newly determined $\log_{10}\beta^\circ$(U(VI)–OH–Si(OH)$_4$) at I_m = 0.05 *m* $NaNO_3$ (solid lines in the figure). The figure underpins the predominance of the $UO_2(OH)_2SiO(OH)_3$ complex in alkaline systems with moderate to high silicate concentrations, whereas no predominance field for the complex $UO_2(OH)_2SiO_2(OH)^2_2$ is predicted.

The shadowed region in the figure denotes the precipitation of SiO_2(am), which was calculated in the absence of uranium with $\log_{10}K^\circ$ (SiO_2(am)) = – 2.71 in (Grenthe et al., 2020). This must be accounted for when defining the stability field of the proposed U(VI)–OH–Si(OH)$_4$ complexes. Note that the use of the hydrolysis constants $\log_{10}\beta^\circ(UO_2(OH)_3)$ and $\log_{10}\beta^\circ(UO_2(OH)^2_4)$ as reported in the solubility study by Altmaier et al. (2017) in combination with the set of consistently derived $\log_{10}\beta^\circ$(U(VI)–OH–Si(OH)$_4$) values results in a slightly different predominance diagram (dashed lines in Fig. 7), which predicts a given predominance field for the complex $UO_2(OH)_2SiO_2(OH)^2_2$. This simulation quantifies the sensitivity of U (VI) speciation to the origin of uranyl hydroxides formation constants used to derive $\log_{10}\beta^\circ$(U(VI)–OH–Si(OH)$_4$).

4. Impact on geochemical assessments

4.1. Implications on the U(VI) uptake in C–S–H phases

Reliable assessment of uranium interaction with cementitious materials is essential in predicting long-term behavior of uranium in cement-based repositories. Although U(IV) is expected to prevail in the reducing conditions developing after repository closure, the stability field of U(VI) significantly expands in hyperalkaline conditions, thus facilitating its possible stabilization in cementitious systems. Calcium silicate hydrate phases (C–S–H) are the main component in hardened cement paste (HCP) and have been described as the main sink of U(VI) in cementitious systems (Tits et al., 2008; Gaona et al., 2012; Wieland, 2014; Ochs et al., 2015). In general, the composition of C–S–H phases is characterized by Ca:Si ratios from 0.7 to 1.7, eventually coexisting with amorphous silica (SiO_2(am)) or portlandite ($Ca(OH)_2$(cr)) at low and high Ca:Si ratios, respectively. Cement degradation is usually categorized into three phases, with stage I characterized by high pH ≥ 13 caused by the dissolution of Na and K oxo-hydroxides, stage II with porewater composition buffered by the dissolution of portlandite at pH ~12.5 and [Ca] ~ 0.02 M, and stage III involving the incongruent dissolution of C–S–H phases and with a pH-evolution from ~12.5 to ~ 10.

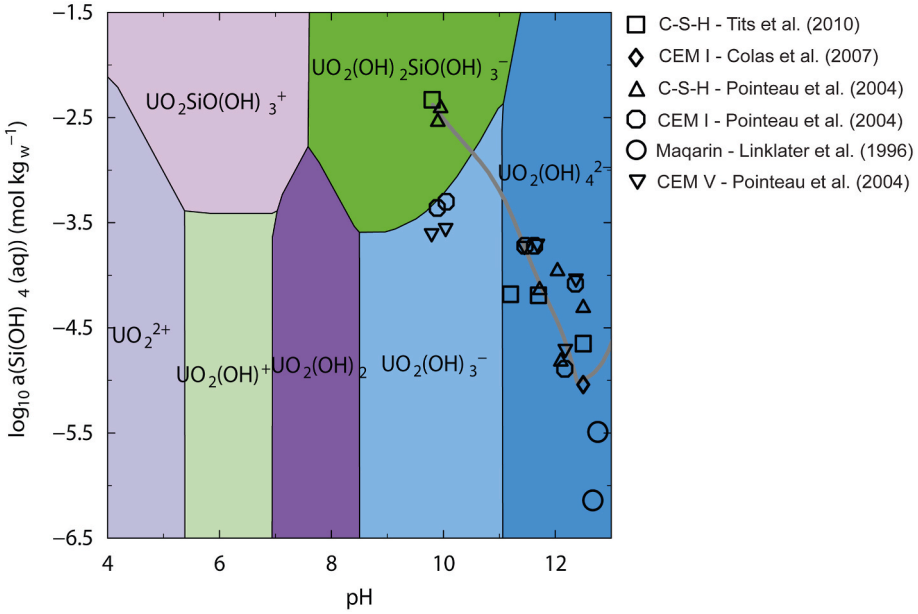

Fig. 8. Predominance plots of U(VI)–OH–Si(OH)$_4$ systems at C(U)$_{tot}$ 10^{-7} mol kg$_w^{-1}$ and I$_m$ 0.1 mol kg$_w^{-1}$ NaCl using NEA-TDB database with the stability constants for uranyl hydroxo silicates species determined in this work. Symbols show experimentally measured [Si] and pH values taken from U[VI] sorption studies on C–S–H phases with different Ca:Si ratios. The thick grey line represents the output of the CASH + model within the pH range of 10–12.5.

Fig. 8 shows the predominance diagram of U(VI) calculated for – 6.5 ≤ log$_{10}$a(Si(OH)$_4$(aq)) ≤ – 0.5 and 4 ≤ pH ≤ 13 using thermodynamic data selected in the NEA-TDB and determined in this work for $UO_2(OH)_2SiO(OH)_3$ and $UO_2(OH)_2SiO_2(OH)_2^{2}$. The anionic hydrolysis species $UO_2(OH)_3$ and $UO_2(OH)_4^{2}$ play a predominant role in the chemistry of U(VI) under alkaline to hyperalkaline systems. In weakly alkaline conditions, the complex $UO_2(OH)_2SiO(OH)_3$ becomes predominant at silicate concentrations as low as 10 ^{3} *m*, whereas greater concentrations are required to outcompete hydrolysis in hyperalkaline conditions. Fig. 8 shows also experimentally measured [Si] and pH values reported in the literature for C–S–H systems of different Ca:Si, as well as their values calculated with the CASH+ model developed by Kulik, Miron and Lothenbach (grey line in the figure) (Kulik, 2011; Miron et al., 2022). It can be inferred that the formation of U(VI)–OH–Si(OH)$_4$ complexes is only expected for the third degradation stage of cement in the form of $UO_2(OH)_2SiO(OH)_3$. In contrast, $UO_2(OH)_2SiO_2(OH)_2^{2}$ species falls outside the scope of relevant cement systems because higher the Si concentrations lead to the formation of C–S–H phases in the presence of Ca.

The uptake mechanism of U(VI) in cementitious systems is believed to commence with an inner-sphere formation through adsorption on the surfaces of the "young" hydrating cement, followed by the formation of solid solution that enhances the uptake in the second stage of degradation (Pointeau et al., 2008). The latter process involves an incorporation of U(VI) in the interlayer structure of C–S–H phases that is anticipated to control the retention of U(VI) in cementitious near-field of a radioactive waste repository (Harfouche et al., 2006). Nevertheless, the specific consideration for anionic U(VI)–OH–Si(OH)$_4$ aqueous species is missing in U(VI) speciation in above-mentioned works. In this study, the obviously longer lifetime of $UO_2(OH)_2SiO_2(OH)_2^{2}$ than $UO_2(OH)_2SiO(OH)_3$ inspires more efforts on the investigation of sorbed or incorporated bidentate silicate as well as on the improvements of the C–S–H solid solution model including U(VI) end-members. The hyperalkaline cement pore water is expected to limit U(VI) mobility by decreasing U(VI) solubility in the degradation stages I and II of C–S–H phases. In the most degraded stage III, the significant loss of Ca^{2+} in the C–S–H phases together with the decrease in pH has a relevant impact on the retention of U(VI) by C–S–H phases (Tits et al., 2011; Gaona et al., 2012).

A further examination of selected samples solutions from U(VI) uptake studies confirms the good prediction of U(VI) sorption isotherms on cementitious materials, regardless of mismatches with data from Maqarin natural analogue sites at hyperalkaline pH values (Linklater et al., 1996). Three samples at pH *ca.* 10 and at [Si] ≈ 4 × 10 ^{3} *m* with a Ca:Si ratio of 0.7–0.75 are identified in the predominance regions of ternary $UO_2(OH)_2SiO(OH)_3$ complex, corresponding to the second and third degradation stages (Pointeau et al., 2004; Tits et al., 2011). Indeed, the likelihood of an equatorial coordination of U(VI) on C–S–H phases with ligands having stronger basicity than OH or with stronger e donors than H_2O has been reported in U(VI) sorption research, using luminescence measurements at 153 K (Tits et al., 2011). Two types of U(VI) species observed at Ca:Si ratios of 0.75 and 1.07, referred to as U(VI)-surface *Type B* and U(VI)-incorporated *Type C*, exhibited clear red-shifts compared to uranyl hydroxides. The authors proposed a bidentate coordination of U(VI) with silica tetrahedron based on the emission characteristics. Current results provide further support for previous observations from an experimental and theoretical viewpoint. Specifically, the agreement between the first emission line of *Type C* species – 505.05 nm (υ_E ≈ 19800 cm ^{1}) in literature and that of theoretically confirmed doubly coordinated U(VI)–OH–Si(OH)$_4$ species strengthens the evidence for the proposed bidentate coordination.

The participation of Ca in the uptake of U(VI) by C–S–H phases remains ill-defined. Tits et al. (2011) suggested a synergistic role of Ca in U(VI) sorption at higher Ca:Si ratios in C–S–H phases. Gaona et al. (2012) derived a solid solution model for the uptake of U(VI) by C–S–H phases, which included Ca–Si–U(VI) end-members prevailing in the interlayer. A recent spectroscopic study identified the sheet-like structure of uranyl silicate mineral – uranophane ($Ca(UO_2)_2SiO_3(OH)_2$ $5H_2O$) in C–S–H phases of low Ca:Si ratio (Yorkshire et al., 2023). While the present study does not address the role of Ca in the formation of ternary U(VI)–OH–Si(OH)$_4$ complexes, the following section included a scale analysis of the interaction between uranyl hydroxides with silicate in the presence of Ca and carbonate considering their importance in the environmental assessment in far-field of nuclear waste repository.

4.2. Case of uranium-carbonate-silicate system

Fig. 9 shows the predominance diagram of uranium in carbonate-silicate domain in the absence of calcium as a function of pH values from 6.5 to 11. The selected pH range is aligned with the pH values commonly encountered in most natural waters, including rare occurrences in alkaline to hyperalkaline environments (Eugster, 1970). Depending on the prevailing conditions such as pH values and concentrations of coexisting ions, the relative importance of carbonate and silicate as competing counterparts for U(VI) varies across different environmental settings. Concerning U(VI)–OH–Si(OH)$_4$ species, the visual results show that either $UO_2SiO(OH)_3^+$ or $UO_2(OH)_2SiO(OH)_3$ dominates the speciation at low carbonate in the pH range of interest. The formation of uranyl hydroxo silicate complexes is generally expected from $\log_{10}a(Si(OH)_4(aq)) \geq -3.5$, while at pH 11, higher silicate concentrations of $\log_{10}a(Si(OH)_4(aq)) \geq -2.2$ are required to outcompete hydrolysis. Noteworthy is that the complexation of polymerized silicic acid with uranium was not considered in the calculation, as there are no available formation constants for U(VI)–OH–$(Si(OH)_4)_n$ complexes in the scientific literature. The inclusion of polysilicic acid in theoretical modelling may have an important impact on the predominant domain of $UO_2(OH)_2SiO(OH)_3$, especially in silicate-rich environments where the formation of nanocolloidal particles have been evidenced (Icopini et al., 2005).

This illustrative exercise demonstrates that the prevalence of uranyl hydroxo silicate complexes is restricted to significantly high concentration of silicate relative to carbonate, which is less frequently observed in the undisturbed geosphere.

Fig. 10 illustrates the evolution of predominance diagrams of the Ca^{2+}–U(VI)–HCO_3–OH –Si(OH)$_4$ system as a function of bicarbonate activity. The horizontal axis $\log_{10}(a(Ca^{2+})/a(H^+)^2)$ allows representing the variation of $Ca(OH)_2$ with the equilibrium written as: $Ca(OH)_2 + 2H^+ \leftrightarrow Ca^{2+} + 2H_2O$. The calculations were conducted at uranium concentration of 10^{-7} *m* and $I_m = 0.1$ *m* NaCl with $\log_{10}a(HCO_3^-)$ varying from – 4 to – 5.5 where one can observe a complete evolutionary transition from Ca–U(VI)–CO_3 to U(VI)–OH–Si(OH)$_4$ complexes with decreasing $\log_{10}a(HCO_3^-)$. The shaded precipitation region of calcite results from the increase of $[Ca^{2+}]\cdot[CO_3^{2-}]$ activity product above the solubility product of calcite, i.e., $\log_{10}K^\circ(\text{calcite}) = -8.48$.

As expected, the decrease of carbonate concentration hampers the precipitation of calcite. The mineral field of calcite was limited by separate calculations in the absence of uranium and silicate using the ht1 (hunt and track) algorithm in Phreeplot, which defines the boundaries of equal number of moles of dissolved Ca^{2+} and precipitated calcite. The $CaCO_3$ mineral fields are sensitive to $\log_{10}a(HCO_3^-)$ especially at high $\log_{10}(a(Ca^{2+})/a(H^+)^2)$. It can be verified that carbonate has a higher affinity than silicate for uranyl ion under neutral to alkaline conditions. The appearance of uranyl hydroxo silicates started from $\log_{10}(a(Si(OH)_4\ (aq)) \approx -3$ at $\log_{10}a(HCO_3^-) = -4.5$ and its predominance increases with decreasing $\log_{10}a(HCO_3^-)$. Meanwhile, one can perceive a rapid loss of significance of U(VI)–CO_3 complexes at lower carbonate concentrations, as shown in Fig. 10 (c, d) where $\log_{10}a(HCO_3^-) = -5, -5.5$. In the calcite-equilibrium system, the low carbonate content requires a high calcium concentration to form calcium uranyl carbonate complexes, which at the same time triggers calcite. The current modelling results imply that depending on the silicate

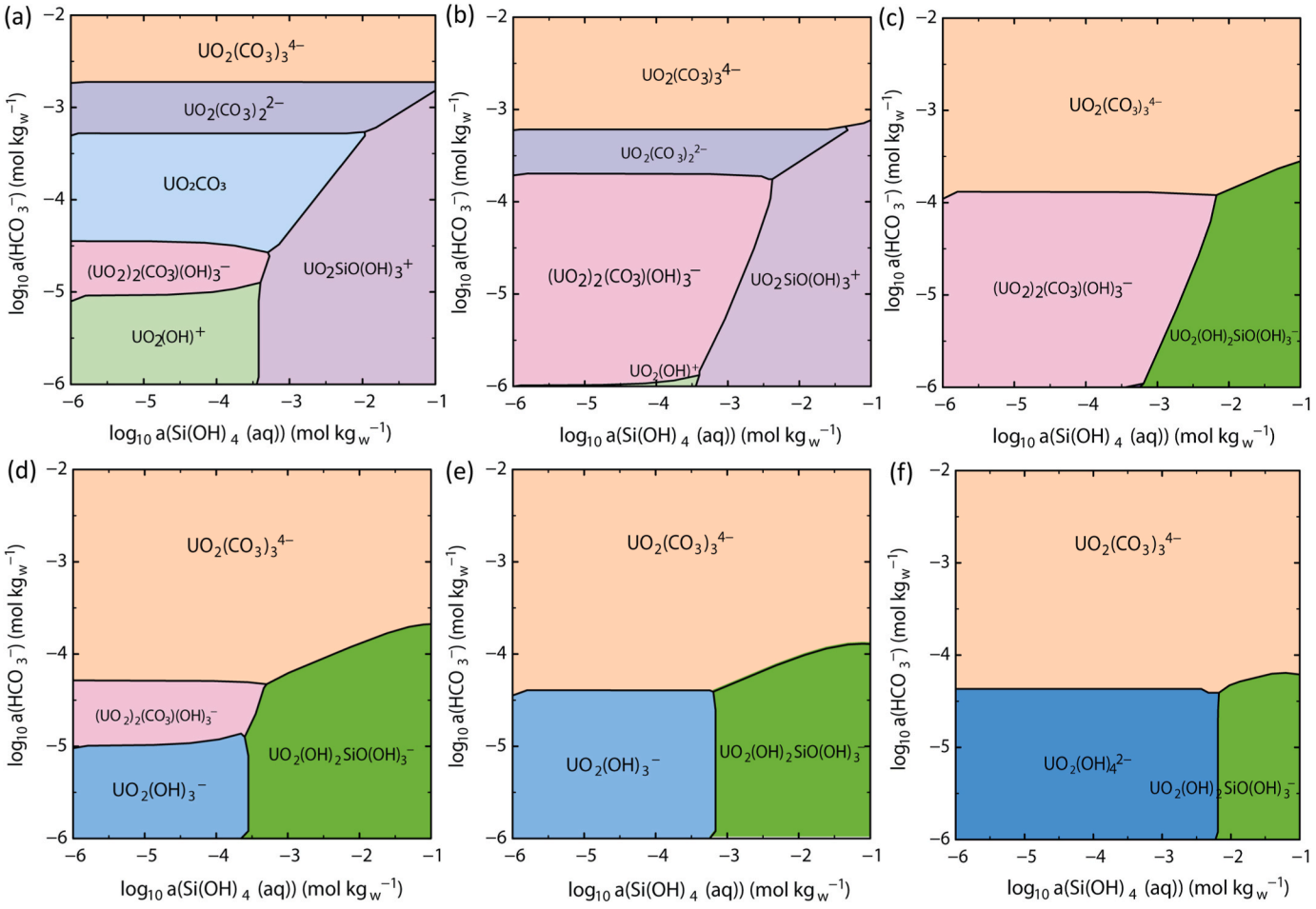

Fig. 9. Predominance diagram of U(VI) aqueous species in the bicarbonate-silicate domain at pH 6.5 (a), pH 7 (b), pH 8 (c), pH 9 (d), pH 10 (e), pH 11 (f) at $C(U)_{tot}$ 10^{-7} mol kg_w^{-1} and I_m 0.1 mol kg_w^{-1} NaCl using NEA-TDB database with the stability constants for uranyl hydroxo silicates species determined in this work.

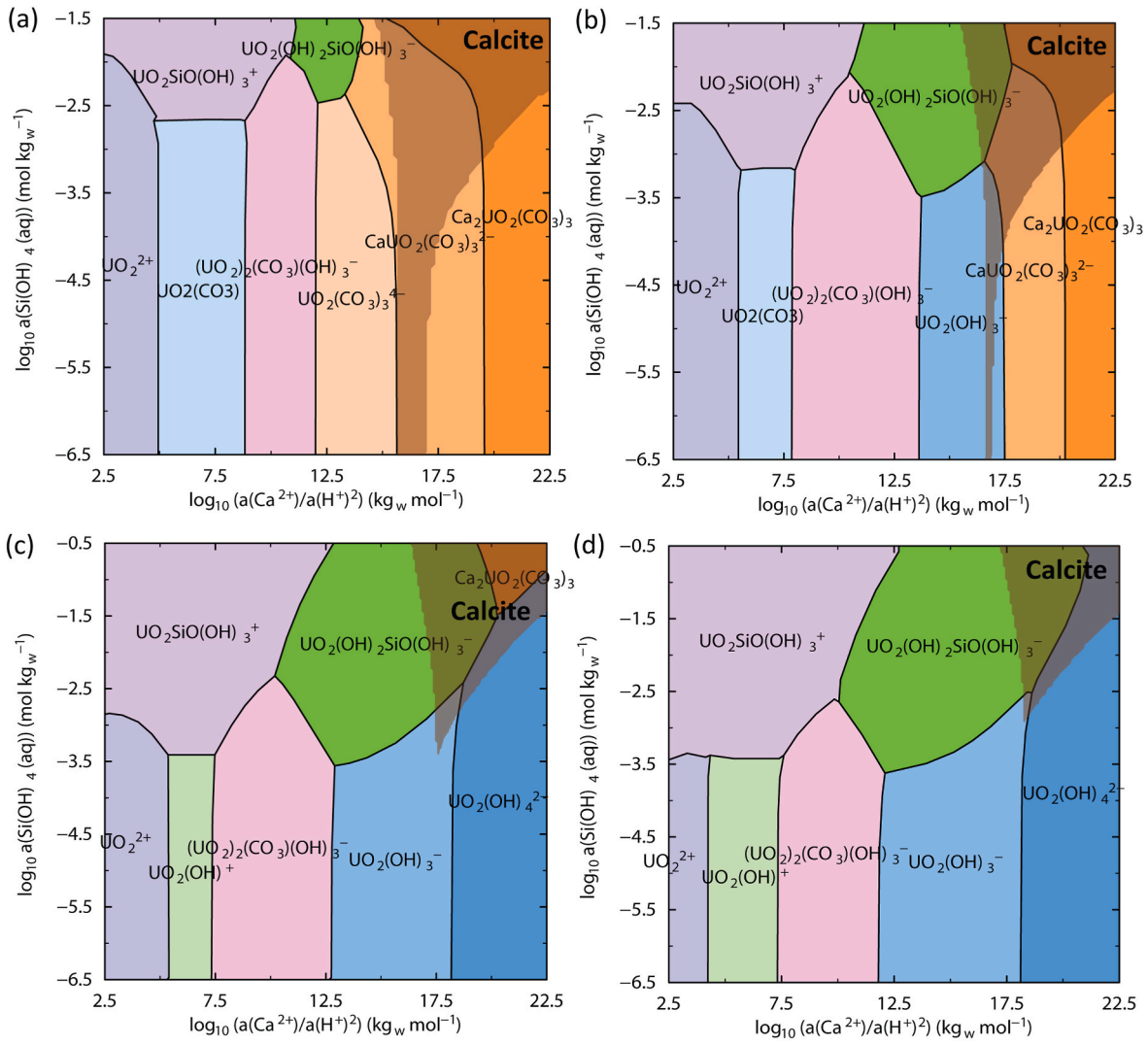

Fig. 10. Activity predominance diagrams of Ca^{2+}–U(VI)–HCO_3^-–OH^-–$Si(OH)_4$ calculated for $C(U)_{tot}$ 10^{-7} mol kg_w^{-1}, $\log_{10}a(HCO_3^-)$ – 4 (a), – 4.5 (b), – 5 (c), – 5.5 (d) at I_m 0.1 mol kg_w^{-1} NaCl using the NEA-TDB database with $\log_{10}\beta^\circ(CaUO_2(CO_3)_3^{2-})$ and $\log_{10}\beta^\circ(Ca_2UO_2(CO_3)_3(aq))$ determined in (Shang and Reiller, 2020). and $\log_{10}\beta^\circ(UO_2(OH)_2SiO(OH)_3^-)$ and $\log_{10}\beta^\circ(UO_2(OH)_2SiO_2(OH)_2^{2-})$ determined in the present work.

concentration, $UO_2(OH)_3$, $UO_2(OH)_4^{2-}$ or $UO_2(OH)_2SiO(OH)_3$ dominates U(VI) speciation at low carbonate concentration under alkaline to hyperalkaline conditions, irrespective of calcium concentration. Gaona et al. also observed the absence of any impact of calcite on the U(VI) uptake in C–S–H phases at high pH, which was attributed to the weak solubilization of calcite imposed by the C–S–H solid solution (Gaona et al., 2012). It is noteworthy that the above discussion as well as the predominance diagrams do not account for the possible formation of quaternary Ca–U(VI)–OH–$Si(OH)_4$ complexes at moderately low $\log_{10}a(HCO_3^-)$. Further experiments could be anticipated to provide more insight into the interaction of Ca^{2+} with negatively charged U(VI)–OH–$Si(OH)_4$ complexes.

In addition, calculated solubility constants of uranyl minerals rely heavily on the thermodynamic stability constants employed in the calculations for the relevant aqueous uranyl complexes. For example, Gorman-Lewis et al. (2008) illustrates a dramatic solubility difference of becquerelite in the presence and absence of aqueous Ca–U(VI)–CO_3 complexes at high pH values. Similarly, sodium boltwoodite gains a higher solubility under acidic conditions than metaschoepite because of the formation of $UO_2SiO(OH)_3^+$. However, as to the extrapolation of solubility curves of uranyl silicate minerals to high pH range, the formation of U(VI)–OH–$Si(OH)_4$ complexes has rarely been accounted in uranophane/Na-boltwoodite/soddyite – related solubility studies due to the lack of reliable thermodynamic constants (Nguyen et al., 1992; Casas et al., 1994; Ilton et al., 2006). It should be noted that the estimation of uranyl minerals solubility at circumneutral to alkaline pH with their stability constants initially determined at low pH values can be significantly impacted by the formation of aqueous complexes at high pH not considered in the chemical model and calculations. The successful determination of $\log_{10}\beta^\circ(UO_2(OH)_2SiO(OH)_3)$ in the current work represents a key contribution for more reliable solubility calculations involving uranyl silicate minerals under alkaline conditions.

5. Conclusions

Equilibrium constants and Gibbs energies of formation of the ternary complexes $UO_2(OH)_2SiO(OH)_3$ and $UO_2(OH)_2SiO_2(OH)_2^{2-}$ were determined at $I_m = 0.05$ *m* $NaNO_3$ under alkaline conditions and extrapolated to infinite dilution with Davies equation. For the first time, the luminescence properties of anionic uranyl hydroxide silicates have been acquired by TRLFS and compared with theoretically-calculated spectra. Slope analysis of spectroscopic data in combination with theoretical calculations provided sound evidence for the stoichiometric number of Si and the coordination mode of silica tetrahedron in the complex

$UO_2(OH)_2SiO(OH)_3$. The longer luminescence lifetime obtained at pH 11.5 compared to lower pH values indicated the formation of a different species, which was tentatively described as $UO_2(OH)_2SiO_2(OH)_2^2$, though inconclusive evidence on the predominance of this complex was obtained from the comparison of experimental and calculated fluorescence spectra. One has to acknowledge the inherent limitations in this study arising from the nature of silicic acid – easy polymerization at high concentration and the hydrolysis of uranyl – strong competition with monosilicates at high pH value. Both complexes exhibited similar patterns in peak positions, which are in good agreement with their corresponding uranyl silicate minerals. A sensitivity analysis was carried out to evaluate the formation of U(VI)–OH–$Si(OH)_4$ species in the alkaline to hyperalkaline conditions expected to predominate in cementitious environments. These calculations predict the predominance of the complex $UO_2(OH)_2SiO(OH)_3$ for the third degradation stage of cement, characterized by moderate alkaline pH (≈ 10) and silicate concentration (≈ 4 × 10^{-3} *m*). On the contrary, the formation of the complex $UO_2(OH)_2SiO_2(OH)_2^2$ is only expected in hyperalkaline conditions with high silicate concentrations and negligible concentrations of Ca. These conditions are neither expected in natural geochemical environments nor in cementitious systems where the higher Ca concentrations promote the formation of C–S–H phases and hence limit silicate concentrations.

The updated thermodynamic model and mechanistic understanding achieved in this study represent a significant improvement for the quantitative description of the solution chemistry of uranium in the alkaline conditions expected in specific repository concepts involving cementitious environments. This research is instrumental in furthering investigations into the interactions of heavy metal ions, e.g. trivalent lanthanides – Eu(III), Cm(III), with silicates under alkaline conditions. Neglecting the formation of U(VI)–OH–$Si(OH)_4$ species may lead to an underestimation of the mobility of related radionuclides upon release and subsequent migration into the vicinity of a clay buffer, particularly in scenarios involving water intrusion into the buffer materials.

CRediT authorship contribution statement

Chengming Shang: Conceptualization, Investigation, Methodology, Writing – original draft, Writing – review & editing. **Xavier Gaona:** Conceptualization, Funding acquisition, Project administration, Supervision, Writing – original draft, Writing – review & editing. **Hanna Oher:** Formal analysis, Software, Writing – original draft. **Robert Polly:** Conceptualization, Writing – review & editing. **Andrej Skerencak-Frech:** Conceptualization, Writing – review & editing. **Sarah Duckworth:** Resources. **Marcus Altmaier:** Conceptualization, Funding acquisition, Project administration, Writing – review & editing.

Declaration of competing interest

The authors declare that they have no known competing financial interests or personal relationships that could have appeared to influence the work reported in this paper.

Data availability

Data will be made available on request.

Acknowledgements

This work is partly funded by the BMWK (Federal Ministry for Economic Affairs and Claimate Action, Germany) within the GraZ II (Geochemical retention of radionuclides and cement alteration phases) project (contract number 02E11860C). Cornelia Beiser and Sylvia Moisei-Rabung are gratefully acknowledged for the ICP–MS/OES measurements and technical support.

Appendix A. Supplementary data

Supplementary data to this article can be found online at https://doi.org/10.1016/j.chemosphere.2023.141048.

References

Ahlrichs, R., Furche, F., Hättig, C., Klopper, W.M., Sierka, M., Weigend, F., 2015. TURBOMOLE v7.0. University of Karlsruhe and Forchungszentrum Karslruhe GmbH.
Alexander, G.B., Heston, W.M., Iler, R.K., 1954. The solubility of amorphous silica in water. J Phys Chem-Us 58, 453–455.
Alexander, W.R., Reijonen, H.M., McKinley, I.G., 2015. Natural analogues: studies of geological processes relevant to radioactive waste disposal in deep geological repositories. Swiss J. Geosci. 108, 75–100.
Altmaier, M., Yalcintas, E., Gaona, X., Neck, V., Müller, R., Schlieker, M., Fanghaenel, T., 2017. Solubility of U(VI) in chloride solutions. I. The stable oxides/hydroxides in NaCl systems, solubility products, hydrolysis constants and SIT coefficients. J. Chem. Thermodyn. 114, 2–13.
Alvarez, R., Sparks, D.L., 1985. Polymerization of silicate anions in solutions at low concentrations. Nature 318, 649–651.
Amayri, S., Reich, T., Arnold, T., Geipel, G., Bernhard, G., 2005. Spectroscopic characterization of alkaline earth uranyl carbonates. J. Solid State Chem. 178, 567–577.
Applin, K.R., 1987. The diffusion of dissolved silica in dilute aqueous solution. Geochem. Cosmochim. Acta 51, 2147–2151.
Arnold, T., Baumann, N., 2009. Boltwoodite [$K(UO_2)(SiO_3OH)(H_2O)_{1.5}$] and compreignacite $K_2[(UO_2)_3O_2(OH)_3]_2{\cdot}7H_2O$ characterized by laser fluorescence spectroscopy. Spectrochimica Acta - Part A: Molecular and Biomolecular Spectroscopy 71, 1964–1968.
Bernhard, G., Geipel, G., Brendler, V., Nitsche, H., 1996. Speciation of uranium in seepage waters of a mine tailing pile studied by time-resolved laser-induced fluorescence spectroscopy (TRLFS). Radiochim. Acta 74, 87–91.
Bilinski, H., Ingri, N., 1967. A determination of the formation constant of $SiO(OH)_3$. Acta Chem. Scand. 21, 2503–2510.
Bostick, B.C., Fendorf, S., Barnett, M.O., Jardine, P.M., Brooks, S.C., 2002. Uranyl surface complexes formed on subsurface media from DOE facilities. Soil Sci. Soc. Am. J. 66, 99–108.
Cao, X., Dolg, M., Stoll, H., 2002. Valence basis sets for relativistic energy-consistent small-core actinide pseudopotentials. J. Chem. Phys. 118, 487–496.
Casas, I., Bruno, J., Cera, E., Finch, R.J., Ewing, R.C., 1994. Kinetic and Thermodynamic Studies of Uranium Minerals Assessment of the Long-Term Evolution of Spent Nuclear Fuel. Sweden, p. 80.
Catalano, J.G., Heald, S.M., Zachara, J.M., Brown, G.E., 2004. Spectroscopic and diffraction study of uranium speciation in contaminated vadose zone sediments from the Hanford site, Washington State. Environ. Sci. Technol. 38, 2822–2828.
Coudurier, M., Baudru, B., Donnet, J., 1971. Étude de la polycondensation de l'acide disilicique. Bull. Soc. Chim. Fr. 9, 3147–3165.
Davies, C.W., 1962. Ion Association. Butterworths, London.
Davis, J.A., Coston, J.A., Kent, D.B., Fuller, C.C., 1998. Application of the surface complexation concept to complex mineral assemblages. Environ. Sci. Technol. 32, 2820–2828.
de Levie, R., 2005. Adanced Excel for Scientific Data Analysis. Oxford University Press, New York.
Deglmann, P., May, K., Furche, F., Ahlrichs, R., 2004. Nuclear second analytical derivative calculations using auxiliary basis set expansions. Chem. Phys. Lett. 384, 103–107.
Di Marco, V.B., Bombi, G.G., 2001. Mathematical functions for the representation of chromatographic peaks. J. Chromatogr. A 931, 1–30.
Dietzel, M., 2000. Dissolution of silicates and the stability of polysilicic acid. Geochem. Cosmochim. Acta 64, 3275–3281.
Drobot, B., Bauer, A., Steudtner, R., Tsushima, S., Bok, F., Patzschke, M., Raff, J., Brendler, V., 2016. Speciation studies of metals in trace concentrations: the mononuclear uranyl(VI) hydroxo complexes. Analytical chemistry 88, 3548–3555.
Drobot, B., Steudtner, R., Raff, J., Geipel, G., Brendler, V., Tsushima, S., 2015. Combining luminescence spectroscopy, parallel factor analysis and quantum chemistry to reveal metal speciation - a case study of uranyl(vi) hydrolysis. Chem. Sci. 6, 964–972.
Drozdzak, J., Leermakers, M., Gao, Y., Elskens, M., Phrommavanh, V., Descostes, M., 2016. Uranium aqueous speciation in the vicinity of the former uranium mining sites using the diffusive gradients in thin films and ultrafiltration techniques. Anal. Chim. Acta 913, 94–103.
Duff, M.C., Amrhein, C., 1996. Uranium (VI) adsorption on goethite and soil in carbonate solutions. Soil Sci. Soc. Am. J. 60, 1393–1400.
Duff, M.C., Amrhein, C., Bertsch, P.M., Hunter, D.B., 1997. The chemistry of uranium in evaporation pond sediment in the San Joaquin Valley, California, USA, using X-ray fluorescence and XANES techniques. Geochem. Cosmochim. Acta 61, 73–81.
Duff, M.C., Morris, D.E., Hunter, D.B., Bertsch, P.M., 2000. Spectroscopic characterization of uranium in evaporation basin sediments. Geochem. Cosmochim. Acta 64, 1535–1550.
Eichkorn, K., Treutler, O., Öhm, H., Häser, M., Ahlrichs, R., 1995. Auxiliary basis sets to approximate Coulomb potentials. Chem. Phys. Lett. 240, 283–290.
Eichkorn, K., Weigend, F., Treutler, O., Ahlrichs, R., 1997. Auxiliary basis sets for main row atoms and transition metals and their use to approximate Coulomb potentials. Theor. Chem. Acc. 97, 119–124.
Eikenberg, J., 1990. On the Problem of Silica Solubility at High pH. Switzerland, p. 57.

Ernzerhof, M., Scuseria, G.E., 1999. Assessment of the Perdew–Burke–Ernzerhof exchange-correlation functional. J. Chem. Phys. 110, 5029–5036.
Eugster, H.P., 1970. Chemistry and origin of the brines of lake Magadi, Kenya. Mineral. Soc. Amer., Spec. Pap. 3, 213–235.
Fanghänel, T., Neck, V., 2002. Aquatic chemistry and solubility phenomena of actinide oxides/hydroxides. Pure Appl. Chem. 74, 1895–1907.
Fleming, B.A., Crerar, D.A., 1982. Silicic acid ionization and calculation of silica solubility at elevated temperature and pH application to geothermal fluid processing and reinjection. Geothermics 11, 15–29.
Froideval, A., Del Nero, M., Gaillard, C., Barillon, R., Rossini, I., Hazemann, J., 2006. Uranyl sorption species at low coverage on Al-hydroxide: TRLFS and XAFS studies. Geochem. Cosmochim. Acta 70, 5270–5284.
Fromentin, E., Reiller, P.E., 2018. Influence of adipic acid on the speciation of Eu(III): review of thermodynamic data in NaCl and $NaClO_4$ media, and a new determination of Eu-adipate complexation constant in 0.5 $mol{\cdot}kg_w^{-1}$ $NaClO_4$ medium by time-resolved luminescence spectroscopy. Inorg. Chim. Acta. 482, 588–596.
Gaona, X., Kulik, D.A., Macé, N., Wieland, E., 2012. Aqueous–solid solution thermodynamic model of U(VI) uptake in C–S–H phases. Appl. Geochem. 27, 81–95.
Gorman-Lewis, D., Burns, P.C., Fein, J.B., 2008. Review of uranyl mineral solubility measurements. J. Chem. Thermodyn. 40, 335–352.
Gorobets, B.S., Engoyan, S.S., Sidorenko, G.A., 1977. Investigation of uranium and uranium-containing minerals by their luminescence spectra. Sov Atom Energy+ 42, 196–202.
Grambow, B., 2006. Nuclear waste glasses - How durable? Elements 2, 357–364.
Greenberg, S.A., 1957. The depolymerization of silica in sodium hydroxide solutions. J Phys Chem-Us 61, 960–965.
Greenberg, S.A., Price, E.W., 1957. The solubility of silica in solutions of electrolytes. J Phys Chem-Us 61, 1539–1541.
Grenthe, I., Fuger, L., Konings, R.G.M., Lemire, R.J., Muller, A.B., Nguyen-Trung, C., Wanner, H., 1992. Chemical Thermodynamics 1. Chemical Thermodynamics of Uranium. North Holland Elsevier Science Publishers B. V., Amsterdam, The Netherlands.
Grenthe, I., Gaona, X., Plyasunov, A.V., Rao, L., Runde, W.H., Grambow, B., Koning, R.J. M., Smith, A.L., Moore, E.E., 2020. Chemical Thermodynamics 14. Second Update on the Chemical Thermodynamics of Uranium, Neptunium, Plutonium, Americium and Technetium. OECD Nuclear Energy Agency Data Bank. OECD Publications, Paris, France.
Guillaumont, R., Fanghänel, T., Neck, V., Fuger, J., Palmer, D.A., Grenthe, I., Rand, M.H., 2003. Update of the Chemical Thermodynamics of Uranium, Neptunium, Plutonium, Americium and Technetium. OECD Nuclear Energy Agency, Data Bank, Issy-les-Moulineaux, France.
Harfouche, M., Wieland, E., Dähn, R., Fujita, T., Tits, J., Kunz, D., Tsukamoto, M., 2006. EXAFS study of U(VI) uptake by calcium silicate hydrates. J. Colloid Interface Sci. 303, 195–204.
Hrnecek, E., Irlweck, K., 1999. Formation of uranium(VI) complexes with monomeric and polymeric species of silicic acid. Radiochim. Acta 87, 29–36.
Hunter, D., Bertsch, P., 1998. In situ examination of uranium contaminated soil particles by micro-X-ray absorption and micro-fluorescence spectroscopies. J. Radioanal. Nucl. Chem. 234, 237–242.
Icopini, G.A., Brantley, S.L., Heaney, P.J., 2005. Kinetics of silica oligomerization and nanocolloid formation as a function of pH and ionic strength at 25°C. Geochem. Cosmochim. Acta 69, 293–303.
Iler, R.K., 1979. The Chemistry of Silica: Solubility, Polymerization, Colloid and Surface Properties and Biochemistry of Silica. Wiley, New York.
Ilton, E.S., Liu, C., Yantasee, W., Wang, Z., Moore, D.A., Felmy, A.R., Zachara, J.M., 2006. The dissolution of synthetic Na-Boltwoodite in sodium carbonate solutions. Geochem. Cosmochim. Acta 70, 4836–4849.
Jensenf, M.P., Choppin, G.R., 1996. Complexation of europium (III) by aqueous orthosilicic acid. Radiochim. Acta 72, 143–150.
Jensenf, M.P., Choppin, G.R., 1998. Complexation of uranyl(VI) by aqueous orthosilicic acid. Radiochim. Acta 82, 83–88.
Kinniburgh, D.G., Cooper, D.M., 2004. Predominance and mineral stability diagrams revisited. Environ. Sci. Technol. 38, 3641–3648.
Kinniburgh, D.G., Cooper, D.M., 2011. PhreePlot: Creating Graphical Output with PHREEQC. http://www.phreeplot.org.
Klamt, A., 1995. Conductor-like screening model for real solvents: a new approach to the quantitative calculation of solvation phenomena. J Phys Chem-Us 99, 2224–2235.
Klamt, A., Jonas, V., 1996. Treatment of the outlying charge in continuum solvation models. J. Chem. Phys. 105, 9972–9981.
Klamt, A., Schüürmann, G., 1993. COSMO: a new approach to dielectric screening in solvents with explicit expressions for the screening energy and its gradient. Journal of the Chemical Society 799–805.
Kouhail, Y.Z., Benedetti, M.F., Reiller, P.E., 2016. Eu(III)-fulvic acid complexation: evidence of fulvic acid concentration dependent interactions by time-resolved luminescence spectroscopy. Environ. Sci. Technol. 50, 3706–3716.
Kouhail, Y.Z., Benedetti, M.F., Reiller, P.E., 2019. Formation of mixed Eu(III)-CO_3-fulvic acid complex: spectroscopic evidence and NICA-Donnan parameters estimation. Chem. Geol. 522, 175–185.
Küchle, W., Dolg, M., Stoll, H., Preuss, H., 1994. Energy-adjusted pseudopotentials for the actinides. Parameter sets and test calculations for thorium and thorium monoxide. J. Chem. Phys. 100, 7535–7542.
Kulik, D.A., 2011. Improving the structural consistency of C-S-H solid solution thermodynamic models. Cement Concr. Res. 41, 477–495.
Lakowicz, J.R., 2006. Principles of Fluorescence Spectroscopy, third ed. Springer, New York.
Linklater, C.M., Albinsson, Y., Alexander, W.R., Casas, I., McKinley, I.G., Sellin, P., 1996. A natural analogue of high-pH cement pore waters from the Maqarin area of northern Jordan: comparison of predicted and observed trace-element chemistry of uranium and selenium. J. Contam. Hydrol. 21, 59–69.
Liu, C., Zachara, J.M., Qafoku, O., McKinley, J.P., Heald, S.M., Wang, Z., 2004. Dissolution of uranyl microprecipitates in subsurface sediments at Hanford Site, USA. Geochem. Cosmochim. Acta 68, 4519–4537.
Lösch, H., 2020. Spectroscopic Studies on the Complexation and Incorporation of Actinides: Uranium(VI) Complexation with Dissolved Silicates and Stability of Europium(III) Xenotim Solid Solutions. Technischen Universität Dresden, Germany.
Lösch, H., Raiwa, M., Jordan, N., Steppert, M., Steudtner, R., Stumpf, T., Huittinen, N., 2020. Temperature-dependent luminescence spectroscopic and mass spectrometric investigations of U(VI) complexation with aqueous silicates in the acidic pH-range. Environ. Int. 136, 105425.
Manov, G.G., Delollis, N.J., Acree, S.F., 1945. Comparative liquid-junction potentials of some pH buffer standards and the calibration of pH meters. J Res Nat Bur Stand 34, 115–127.
Marshall, W.L., 1980. Amorphous silica solubilities—I. Behavior in aqueous sodium nitrate solutions; 25–300°C, 0–6 molal. Geochem. Cosmochim. Acta 44, 907–913.
Marshall, W.L., Warakomski, J.M., 1980. Amorphous silica solubilities—II. Effect of aqueous salt solutions at 25°C. Geochem. Cosmochim. Acta 44, 915–924.
Martínez-Torrents, A., Meca, S., Baumann, N., Martí, V., Giménez, J., de Pablo, J., Casas, I., 2013. Uranium speciation studies at alkaline pH and in the presence of hydrogen peroxide using time-resolved laser-induced fluorescence spectroscopy. Polyhedron 55, 92–101.
Mei, H., Tan, X., Yu, S., Ren, X., Chen, C., Wang, X., 2015. Effect of silicate on U(VI) sorption to γ-Al_2O_3: batch and EXAFS studies. Chem. Eng. J. 269, 371–378.
Miller, W., Alexander, R., Chapman, N., McKinley, J.C., Smellie, J., 2000. Geological Disposal of Radioactive Wastes and Natural Analogues. Elsevier, Oxford.
Miron, G.D., Kulik, D.A., Yan, Y., Tits, J., Lothenbach, B., 2022. Extensions of CASH+ thermodynamic solid solution model for the uptake of alkali metals and alkaline earth metals in C-S-H. Cement Concr. Res. 152, 106667.
Moll, H., Geipel, G., Brendler, V., Bernhard, G., Nitsche, H., 1998. Interaction of uranium (VI) with silicic acid in aqueous solutions studied by time-resolved laser-induced fluorescence spectroscopy (TRLFS). J Alloy Compd 271–273, 765–768.
Moreau, P., Colette-Maatouk, S., Vitorge, P., Gareil, P., Reiller, P.E., 2015. Complexation of europium(III) by hydroxybenzoic acids: a time-resolved luminescence spectroscopy study. Inorg. Chim. Acta. 432, 81–88.
Moriyasu, M., Yokoyama, Y., Ikeda, S., 1977. Quenching of uranyl luminescence by water molecule. J. Inorg. Nucl. Chem. 39, 2211–2214.
Morris, D.E., Allen, P.G., Berg, J.M., Chisholm-Brause, C.J., Conradson, S.D., Donohoe, R. J., Hess, N.J., Musgrave, J.A., Tait, C.D., 1996. Speciation of uranium in Fernald soils by molecular spectroscopic methods: characterization of untreated soils. Environ. Sci. Technol. 30, 2322–2331.
Moulin, C., Beaucaire, C., Decambox, P., Mauchien, P., 1990. Determination of uranium in solution at the ng l^{-1} level by time-resolved laser-induced spectrofluorimetry: application to geological samples. Anal. Chim. Acta 238, 291–296.
Moulin, C., Decambox, P., Moulin, V., Decaillon, J.G., 1995. Uranium speciation in solution by time-resolved laser-induced fluorescence. Analytical chemistry 67, 348–353.
Mysen, B., Richet, P., 2018. Silicate Glasses and Melts. Elsevier Science.
Nguyen, S.N., Silva, R.J., Weed, H.C., Andrews, J.E., 1992. Standard Gibbs free energies of formation at the temperature 303.15 K of four uranyl silicates: soddyite, uranophane, sodium boltwoodite, and sodium weeksite. J. Chem. Thermodyn. 24, 359–376.
Nizhegorodov, N.I., 1992. Effect of molecule symmetry on fluorescence parameters and on the intercombination conversion constant. J. Appl. Spectrosc. 57, 873–878.
Ochs, M., Mallants, D., Wang, L., 2015. Radionuclide and Metal Sorption on Cement and Concrete. Springer Cham, Switzerland.
Oher, H., Ferru, G., Couston, L., Berthon, L., Guillaumont, D., Réal, F., Vercouter, T., Vallet, V., 2022. Influence of the first coordination of uranyl on its luminescence properties: a study of uranyl binitrate with N,N-Dialkyl Amide DEHiBA and water. Inorg. Chem. 61, 890–901.
Oher, H., Gomes, A.S.P., Wilson, R.E., Schnaars, D.D., Vallet, V., 2023. How does bending the uranyl unit influence its spectroscopy and luminescence? Inorg. Chem. 62, 9273–9284.
Oher, H., Réal, F., Vercouter, T., Vallet, V., 2020a. Investigation of the luminescence of $[UO_2X_4]^{2-}$ (X = Cl, Br) complexes in the organic phase using time-resolved laser-induced fluorescence spectroscopy and quantum chemical simulations. Inorg. Chem. 59, 5896–5906.
Oher, H., Vercouter, T., Réal, F., Shang, C., Reiller, P.E., Vallet, V., 2020b. Influence of alkaline earth metal ions on structures and luminescent properties of $Na_mM_nUO_2(CO_3)_3^{(4-m-2n)-}$ (M = Mg, Ca; m, n = 0–2): time-resolved fluorescence spectroscopy and *ab initio* studies. Inorg. Chem. 59, 15036–15049.
Panak, P.J., Kim, M.A., Klenze, R., Kim, J.-I., Fanghänel, T., 2005. Complexation of Cm (III) with aqueous silicic acid. Radiochim. Acta 93, 133–139.
Parkhurst, D.L., Appelo, C.A.J., 1999. User's Guide to PHREEQC (version 2) — a computer program for speciation. Batch-Reaction, One-Dimensional Transport, and Inverse Geochemical Calculations. U.S. Geological Survey, Water-Resources Investigations, Lakewood, Colorado, USA.
Parkhurst, D.L., Appelo, C.A.J., 2013. Description of Input and Examples for PHREEQC Version 3 — A Computer Program for Speciation, Batch-Reaction, One-Dimensional Transport, and Inverse Geochemical Calculations. U.S. Geological Survey, Denver, Colorado, USA (Chapter 43) of Section A, Groundwater Book 6, Modeling Techniques.

Parr, R.G., Pearson, R.G., 1983. Absolute hardness: companion parameter to absolute electronegativity. J. Am. Chem. Soc. 105, 7512–7516.
Pathak, P.N., Choppin, G.R., 2006. Thermodynamic study of metal silicate complexation in perchlorate media. Radiochim. Acta 94, 81–86.
Payne, T.E., Waite, T.D., 1991. Surface complexation modelling of uranium sorption data obtained by isotope exchange techniques. Radiochim. Acta 52, 487–494.
Pointeau, I., Coreau, N., Reiller, P., 2008. Uptake of anionic radionuclides onto degraded cement pastes and competing effect of organic ligands. Radiochim. Acta 96, 367.
Pointeau, I., Landesman, C., Giffaut, E., Reiller, P., 2004. Reproducibility of the uptake of U(VI) onto degraded cement pastes and calcium silicate hydrate phases. Radiochim. Acta 92, 645–650.
Porter, R.A., Weber, W.J., 1971. The interaction of silicic acid with iron(III) and uranyl ions in dilute aqueous solution. J. Inorg. Nucl. Chem. 33, 2443–2449.
Reiller, P.E., Vercouter, T., Duro, L., Ekberg, C., 2011. Thermodynamic data provided through the FUNMIG project: analyses and prospective. Appl. Geochem. 27, 414–426.
Riley, R.G., 1992. Chemical Contaminants on DOE Lands and Selection of Contaminant Mixtures for Subsurface Science Research. US Department of Energy, Office of Energy Research, Subsurface Science Program.
Rinder, T., Oelkers, E.H., 2014. On the colorimetric measurement of aqueous Si in the presence of organic ligands and common pH buffering agents. Mineral. Mag. 78, 1431–1436.
Saito, T., Aoyagi, N., Kimura, T., 2015. Time-resolved laser-induced fluorescence spectroscopy combined with parallel factor analysis: a robust speciation technique for UO_2^{2+}. J. Radioanal. Nucl. Chem. 303, 1129–1132.
Satoh, I., Choppin, G.R., 1992. Interaction of uranyl(VI) with silicic acid. Radiochim. Acta 56, 85–88.
Schäfer, A., Horn, H., Ahlrichs, R., 1992. Fully optimized contracted Gaussian basis sets for atoms Li to Kr. J. Chem. Phys. 97, 2571–2577.
Schwartzentruber, J., Fürst, W., Renon, H., 1987. Dissolution of quartz into dilute alkaline solutions at 90°C: a kinetic study. Geochem. Cosmochim. Acta 51, 1867–1874.
Shang, C., Reiller, P., 2021. Thermodynamic constant of $MgUO_2(CO_3)_3^{2-}$ complex in $NaClO_4$ and NaCl media using time-resolved luminescence spectroscopy, and applications to different geochemical contexts. Dalton Trans. 50, 4363–4379.
Shang, C., Reiller, P.E., 2020. Determination of formation constants and specific ion interaction coefficients for $Ca_nUO_2(CO_3)_3^{(4-2n)-}$ complexes in NaCl solution by time-resolved laser-induced luminescence spectroscopy. Dalton Trans. 49, 466–481.
Shang, C., Reiller, P.E., Vercouter, T., 2020. Spectroluminescence measurements of stability constants of $Ca_nUO_2(CO_3)_3^{(4-2n)-}$ complexes in $NaClO_4$ medium and investigation of interaction effects. Dalton Trans. 49, 15443–15460.
Shilov, V.P., Fedoseev, A.M., Yusov, A.B., Delegard, C.H., 2004. Behavior of Np(VII, VI, V) in silicate solutions. Radiochemistry 46, 574–577.
Sjöberg, S., 1996. Silica in aqueous environments. J. Non-Cryst. Solids 196, 51–57.
Su, J., Wang, Y.-L., Wei, F., Schwarz, W.H.E., Li, J., 2011. Theoretical study of the luminescent states and electronic spectra of UO_2Cl_2 in an argon matrix. J. Chem. Theor. Comput. 7, 3293–3303.
Su, J., Wang, Z., Pan, D., Li, J., 2014. Excited states and luminescent properties of UO_2F_2 and its solvated complexes in aqueous solution. Inorg. Chem. 53, 7340–7350.
Tanaka, M., Takahashi, K., 2001. Silicate species in high pH solution molybdate, whose silica concentration is determined by colorimetry. Anal. Chim. Acta 429, 117–123.
Tecmer, P., Bast, R., Ruud, K., Visscher, L., 2012. Charge-transfer excitations in uranyl tetrachloride ($[UO_2Cl_4]^{2-}$): How reliable are electronic spectra from relativistic time-dependent density functional theory? J. Phys. Chem. A 116, 7397–7404.
Thakur, P., Singh, D.K., Choppin, G.R., 2007. Polymerization study of o-$Si(OH)_4$ and complexation with Am(III), Eu(III) and Cm(III). Inorg. Chim. Acta. 360, 3705–3711.
Tits, J., Fujita, T., Tsukamoto, M., Wieland, E., 2008. Uranium(VI) uptake by synthetic calcium silicate hydrates. MRS Online Proc. Libr. 1107, 467.
Tits, J., Geipel, G., Macé, N., Eilzer, M., Wieland, E., 2011. Determination of uranium(VI) sorbed species in calcium silicate hydrate phases: a laser-induced luminescence spectroscopy and batch sorption study. J. Colloid Interface Sci. 359, 248–256.
Treutler, O., Ahlrichs, R., 1995. Efficient molecular numerical integration schemes. J. Chem. Phys. 102, 346–354.
van Lenthe, E., Baerends, E.J., 2003. Optimized Slater-type basis sets for the elements 1–118. J. Comput. Chem. 24, 1142–1156.
van Lenthe, E., Baerends, E.J., Snijders, J.G., 1993. Relativistic regular two-component Hamiltonians. J. Chem. Phys. 99, 4597–4610.
van Lier, J.A., de Bruyn, P.L., Overbeek, J.T.G., 1960. The solubility of quartz. J Phys Chem-Us 64, 1675–1682.
Vercouter, T., 2005. Complexes aqueux de lanthanides(III) et actinides(III) avec les ions carbonate et sulfate. Etude thermodynamique par spectrofluorimétrie laser résolue en temps et spectrométrie de masse à ionisation électrospray. Université Evry Val d'Essonne, Evry, France.
Vercouter, T., Amekraz, B., Moulinfi, C., 2009a. Silicate complexation of trivalent lanthanides and actinides. Wissenschaftliche Berichte FZKA 7461, 367–374.
Vercouter, T., Casanova, F., Calvo, A., Amekraz, B., Moulin, C., 2009b. Influence of silicate ions on Eu(III) aqueous speciation. 4th Ann. Workshop Proc. Of Integrated Project "Fundamental Processes of Radionuclide Migration"(6th EC FP IP FUNMIG). Report FZKA, pp. 263–270.
Vochten, R., Blaton, N., Peeters, O., van Springel, K., van Haverbeke, L., 1997. A new method of synthesis of boltwoodite and of formation of sodium boltwoodite, uranophane, sklodowskite and kasolite from boltwoodite. Can. Mineral. 35, 735–741.
von Arnim, M., Ahlrichs, R., 1999. Geometry optimization in generalized natural internal coordinates. J. Chem. Phys. 111, 9183–9190.
Wadsak, W., Hrnecek, E., Irlweck, K., 2000. Formation of americium(III) complexes with aqueous silicic acid. Radiochim. Acta 88, 61–64.
Waite, T., Davis, J., Payne, T., Waychunas, G., Xu, N., 1994. Uranium(VI) adsorption to ferrihydrite: application of a surface complexation model. Geochem. Cosmochim. Acta 58, 5465–5478.
Wang, Z., Felmy, A.R., Xia, Y., Qafoku, O., Yantassee, W., Cho, H., 2005a. Complexation of Cm(III)/Eu(III) with silicates in basic solutions. Radiochim. Acta 93, 741–748.
Wang, Z., Zachara, J.M., Liu, C., Gassman, P.L., Felmy, A.R., Clark, S.B., 2008. A cryogenic fluorescence spectroscopic study of uranyl carbonate, phosphate and oxyhydroxide minerals. Radiochim. Acta 96, 591–598.
Wang, Z., Zachara, J.M., Yantasee, W., Gassman, P.L., Liu, C., Joly, A.G., 2004. Cryogenic laser induced fluorescence characterization of U(VI) in Hanford vadose zone pore waters. Environ. Sci. Technol. 38, 5591–5597.
Wang, Z., Zachara, J.M.G., Paul, L., Liu, C., Qafoku, O., Yantasee, W., Catalano, J.G., 2005b. Fluorescence spectroscopy of U(VI) silicates and U(VI) contaminated Hanford sediment. Geochem. Cosmochim. Acta 69, 1391–1403.
Wanner, H., Östhols, E., 1999. Guidelines for the Assignement of Uncertainties. Issy-les-Moulineaux, France.
Weigend, F., Ahlrichs, R., 2005. Balanced basis sets of split valence, triple zeta valence and quadruple zeta valence quality for H to Rn: Design and assessment of accuracy. Phys. Chem. Chem. Phys. 7, 3297–3305.
Weigend, F., Häser, M., Patzelt, H., Ahlrichs, R., 1998. RI-MP2: optimized auxiliary basis sets and demonstration of efficiency. Chem. Phys. Lett. 294, 143–152.
Wieland, E., 2014. Sorption data base for the cementitious near-field of L/ILW and ILW repositories for provisional safety analyses for SGT-E2. In: Medium: X. Paul Scherrer Institute (PSI), Villigen (Switzerland), Switzerland. Size: 142 page(s).
Yanai, T., Tew, D.P., Handy, N.C., 2004. A new hybrid exchange–correlation functional using the Coulomb-attenuating method (CAM-B3LYP). Chem. Phys. Lett. 393, 51–57.
Yorkshire, A.S., Stennett, M.C., Walkley, B., Provis, J.L., Townsend, L.T., Haigh, L.T., Hyatt, N.C., Mottram, L.M., Corkhill, C.L., 2023. Spectroscopic identification of Ca-bearing uranyl silicates formed in C–S–H systems. Sci Rep-Uk 13, 3374.
Yusov, A.B., Fedoseev, A.M., 2003. Reaction of plutonium(VI) with orthosilicic acid Si$(OH)_4$. Russ. J. Coord. Chem. 29, 582–590.
Yusov, A.B., Fedoseev, A.M., 2005. A spectrophotometric study of the interaction of uranyl ions with orthosilicic acid and polymeric silicic acids in aqueous solutions. Radiochemistry 47, 345–351.
Yusov, A.B., Fedoseev, A.M., Isakova, O.V., Delegard, C.H., 2005. Complexation of Np(V) with silicate ions. Radiochemistry 47, 39–44.